*applied sciences*

MDPI

*Review*

# Dynamics of Long-Runout Landslides: A Review

**Zhen Lei [1,2], Wuwei Mao [3] and Fangwei Yu [1,2,*]**

[1] Institute of Mountain Hazards and Environment, Chinese Academy of Sciences, Chengdu 610213, China; leizhen@imde.ac.cn
[2] University of Chinese Academy of Sciences, Beijing 100049, China
[3] Department of Geotechnical Engineering, College of Civil Engineering, Tongji University, Shanghai 200092, China; maowuwei@tongji.edu.cn
* Correspondence: fwyuui@gmail.com

**Abstract**

Long-runout landslides usually cause a significant loss of life and property because of their hypermobility and immense energy to travel long distances at high velocities, attracting a global focus on the dynamics and mechanism of long-runout landslides. In the past few decades, a great number of past studies on long-runout landslides have seen a surge in a range of innovative ideas and vigorous debates contributing to the advancement of understanding the dynamics and mechanism of the hypermobility of long-runout landslides. As a consequence, a review of the dynamics of long-runout landslides has been conducted by comprehensively and systematically summarizing the data and achievements of long-runout landslides over the past few decades in terms of the phenomenon and characteristics, mobility, dynamic process, dynamic mechanism, and models of long-runout landslides. This review would be of great significance in providing a comprehensive reference in understanding the dynamics of long-runout landslides.

**Keywords:** dynamics; dynamic mechanisms; dynamic models; long-runout landslides; mobility

check for updates

Academic Editor: Cheng-Yu Ku

Received: 2 September 2025
Revised: 28 September 2025
Accepted: 2 October 2025
Published: 22 October 2025

**Citation:** Lei, Z.; Mao, W.; Yu, F. Dynamics of Long-Runout Landslides: A Review. *Appl. Sci.* **2025**, *15*, 11300. https://doi.org/10.3390/app152111300

**Copyright:** © 2025 by the authors. Licensee MDPI, Basel, Switzerland. This article is an open access article distributed under the terms and conditions of the Creative Commons Attribution (CC BY) license (https://creativecommons.org/licenses/by/4.0/).

## 1. Introduction

Recently, landslides, as a kind of significant geomorphological process responsible for gravity-driven geological disasters, have attracted global attention due to their complex dynamic mechanisms and evolutions [1–4]. This focus is especially prominent in the case of long-runout landslides, which are characterized by their high velocity, extensive long-runout distance, and immense energy, potentially causing significant damage to life, property, and infrastructure [5–9]. In general, landslides are defined as the downward movement of rock and soil masses driven by gravitational force. The term 'landslides' is a collective designation encompassing both 'rockfalls' and 'debris flows' [10]. However, both domestically and internationally, there is no precise or universally accepted definition of landslides.

According to the "Recommended Method for Describing Long-runout Landslide Displacement Velocities" released by the "International Geosciences Union Landslide Working Group" in 1995, landslides are categorized into seven levels by their displacement velocities: "extremely slow, very slow, slow, moderate, fast, very fast, and extremely fast" [11]. The displacement velocity of the extremely fast landslide ranges from the lower limit of 5 m/s to the upper limit of 70 m/s. At present, the average velocities of long-runout landslides are considered to exceed 20 m/s, fall into the category of extremely fast

landslide [6]. The long-runout landslides addressed in this paper, with their displacement velocities typically exceeding 30 m/s, greatly surpass the lower limit of the displacement velocity of extremely fast landslides.

Internationally, the equivalent friction coefficient $\mu$ of the landslide is defined as the ratio of the maximum vertical displacement of the landslide, $H_{max}$, to the maximum horizontal displacement of the landslide, $L_{max}$ [1–3], i.e., $\mu = H_{max}/L_{max}$, is generally used to determine if the landslide is quantified as a long-runout landslide. In fact, the equivalent friction coefficient of a landslide can be defined more reasonably by the ratio of the vertical displacement of the landslide's center of mass $H_G$ to the horizontal displacement of the landslide's center of mass $L_G$, i.e., $H_G/L_G$, to replace the ratio $H_{max}/L_{max}$ of the landslide, to interpret the mobility of the landslide by its center of mass. In comparison with the ratio $H_{max}/L_{max}$ of landslide, the ratio $H_{max}/L_{max}$ of landslide is more commonly used to quantify its mobility because of the accessibility of $H_{max}$ and $L_{max}$ of landslide. In general, the landslide is classified as a long-runout landslide when its $H_{max}/L_{max}$ is less than 0.6, as illustrated in Figure 1.

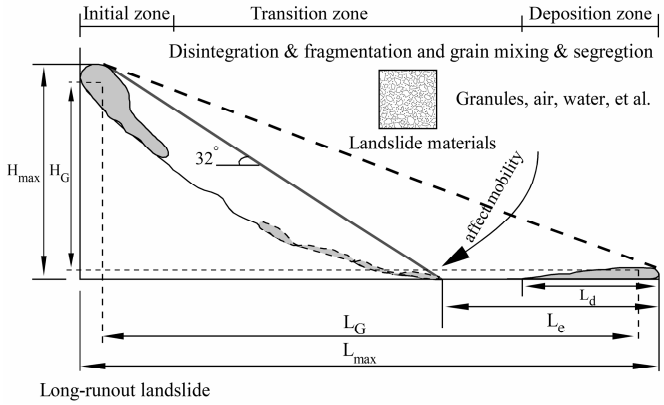



**Figure 1.** Illustration of the mobility of a long-runout landslide. ($H_G$: the vertical displacement of the center of mass, $L_G$: the horizontal movement distance of the center of mass, $H_{max}$: the maximum vertical drop, $L_{max}$: the maximum runout distance, $L_d$: the deposition distance (also called $L_s$), and $L_e$: the extended runout distance).

Studying the dynamics and mechanisms of long-runout landslides is of significant scientific importance for reducing damage to human lives and regional economies. Despite extensive research, no universally applicable theory has been developed to fully characterize these complex processes. This study presents the state of the art on the long-runout landslide dynamics by reviewing a vast body of literature, providing a valuable reference for future research in the field.

## 2. Phenomenon and Characteristics of Long-Runout Landslides

### *2.1. Phenomenon of Long-Runout Landslides*

The study of long-runout landslides began in 1932 with Heim's pioneering analysis of the 1881 Elm landslide in Switzerland [12]. Heim and Buss [13] categorized the Elm landslide into three distinct stages: collapse, jump, and torrent. The collapsing mass collided with the foot of the slope, generating a debris flow, which flowed in a torrent like form on a nearly horizontal slope for almost 1.5 km. The resulting deposits were tongue-shaped, similar to deposits of debris flows and other fluids [13]. Heim and Buss [13] highlighted that the unexpected long-distance travel of the debris flow in the Elm landslide, which was unexpected, was responsible for the majority of fatalities. In subsequent studies, Heim [12] suggested that the debris flow in the Elm landslide behaved similarly to granular fluids or

debris flows, with particle collisions being the main mechanism for force transmission in the debris flow.

The exceptionally high velocities and long-runout distances of long-runout landslides frequently result in catastrophic events. The 1881 Elm landslide in Switzerland involved a debris flow with a volume of $1.1 \times 10^7$ m$^3$, which traveled 1.5 km at an average speed of 42 m/s, burying an entire village and causing 120 fatalities [12,13]. In 1962, a landslide with a volume of $1.3 \times 10^7$ m$^3$ occurred in Peru's Ancash Province, completely burying the village of Ranrahirca and causing 5000 fatalities [14]. On 8 October 2005, the Kashmir earthquake triggered the largest Hattian Bala long-runout landslide with a volume of $6.8 \times 10^7$ m$^3$, which traveled approximately 2.6 km horizontally after destabilizing, burying a village and causing over 1000 fatalities [15]. In China, many famous catastrophic long-runout landslides have occurred from 1960s to the 21st century, e.g., the large long-runout landslide in the Pudu River Valley of Yunnan buried five villages, causing 444 deaths in 1965 [16]; In 1989, a long-runout landslide in Xikou Town in Sichuan, resulted in 221 fatalities [17]; In 2000, a massive landslide occurred in the Yigong Zangbo River in Tibet [18,19]; During 2008 Wenchuan "5.12" earthquake, due to the fragile geological environment in the Longmenshan high mountains, coupled with the earthquake's extended duration (about 120 s) and strong ground shaking (peak ground acceleration up to 1.5–2.0 g), numerous long-runout landslides were triggered, causing an extraordinary amount of damage [20]. As a result, understanding the dynamics of long-runout landslides, and predicting their velocity, runout distance, impact force, and coverage area, is of tremendous importance for the development of mountainous areas and the protection of life safety.

### 2.2. Characteristics of Long-Runout Landslides

A hallmark of long-runout landslides is that their travel distance is significantly greater than what is predicted by the simple friction models [1,6]. The renowned geologist Heim was the first to document this hypermobility during his study of the 1881 Elm landslide in Switzerland [12]. This pioneering work garnered significant attention, focusing on the remarkable flowability of long-runout landslides [1,5,12].

As demonstrated in Figure 2, the larger volume of long-runout landslides is shown to generally result in a higher mobility by a smaller apparent friction coefficient to travel in a greater runout distance, i.e., the apparent friction coefficient of a landslide decreases to flow farther while increasing its volume.

Long-runout landslides can be characterized usually by the following features:

(1) Hypermobility: Long-runout landslides, typically characterized by a volume exceeding $1 \times 10^6$ m$^3$, are usually to travel in an excessively long horizontal runout distance, being characterized by an ultralow equivalent friction coefficient (i.e., $\mu = H_{max}/L_{max}$) that is usually much lower than 0.6, causing a high-speed flow-like behavior of long-runout landslides to travel in a long runout distance [1,3,7,21].

(2) Disintegration and fragmentation: In the gravity-driven geophysical process of long-runout landslides, landslide mass disintegration and fragmentation are usually accompanied by the dynamic process of granular flow formation [2,22–26].

(3) Grain segregation: By following the dynamic process of the disintegration and fragmentation of landslide mass, long-runout landslide is gradually transformed into granular flow that usually causes a phenomenon of grain segregation, i.e., a gravity-driven inverse grading structure of granular material where the particle size distribution coarsens upwards (i.e., large grains over small grains), which has been verified in the in-site long-runout landslides [7,22,27–30].

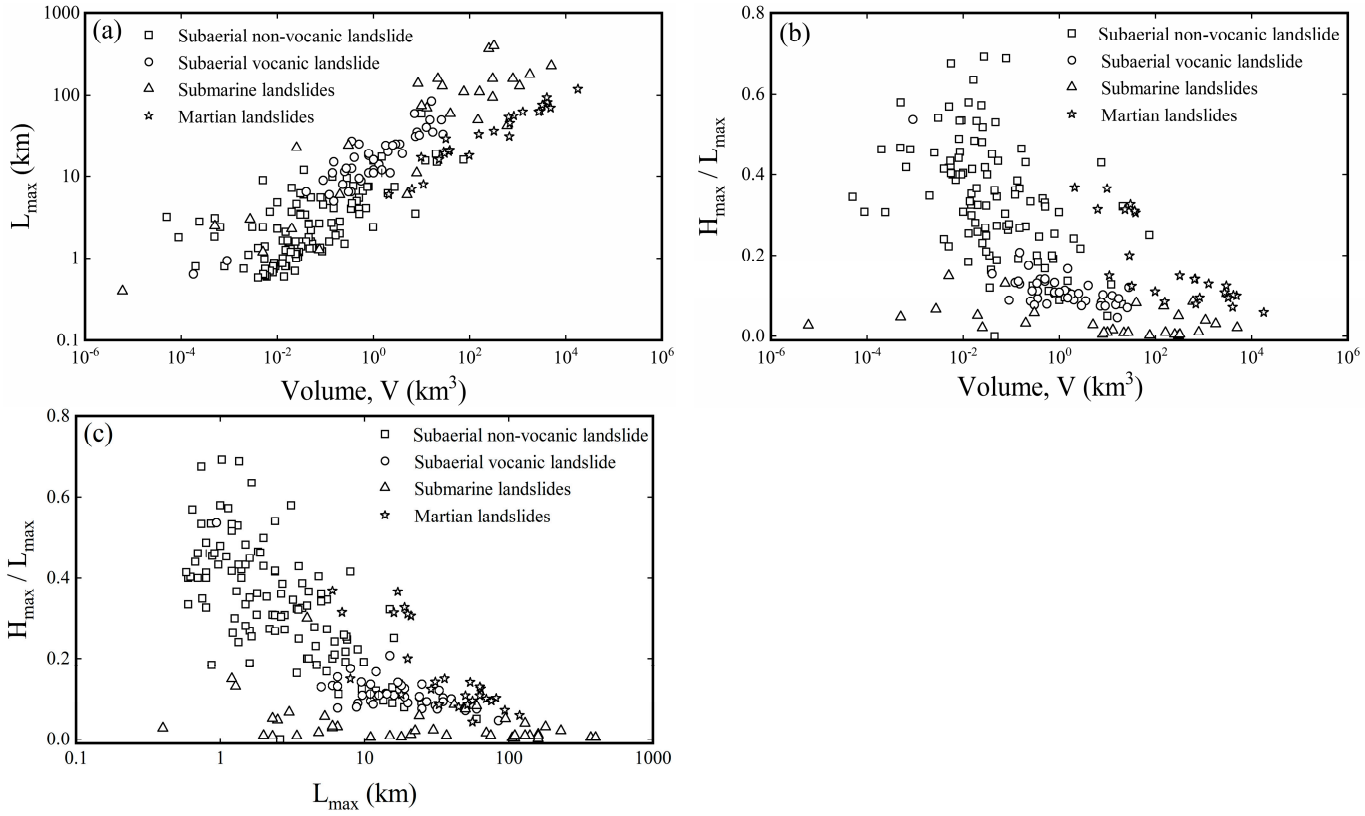



**Figure 2.** Mobility of long-runout landslides: (**a**) Relation of the maximum runout distance ($L_{max}$) and volume; (**b**) Relation of the equivalent friction coefficient $\mu$ ($H_{max}$ / $L_{max}$) and volume; (**c**) Relation of the maximum runout distance ($L_{max}$) and the equivalent friction coefficient $\mu$ ($H_{max}$ / $L_{max}$). Data sourced from Appendix Table A1. Equations of the best power-law fit to each set of data are presented in Appendix Table A2.

## 3. Mobility of Long-Runout Landslides

### *3.1. Role of Dynamic Disintegration and Fragmentation on Mobility of Long-Runout Landslides*

The gravity-driven geophysical process of long-runout landslides is characterized by dynamic disintegration and fragmentation of the landslide mass, resulting in the formation of a granular flow that traverses long distances [2,9,23,26,31]. Consequently, the dynamic disintegration and fragmentation of landslide mass is a significant factor in the mobility of long-runout landslides [2,22–24,32,33].

Initially, particle fragmentation was believed to enhance the mobility of long-runout landslides by reducing particle size and expanding volume, leading to a rapid rise in fluidization [22,23,33,34]. However, later studies shifted focus toward characterizing particle fragmentation [2,35–38]. Moreover, some researchers have begun integrating particle fragmentation characteristics into landslide studies to explore its impact on landslide mobility [2,24,32,33,39].

As demonstrated by Wang et al. [39], the landslide at Hiegaesi was simulated to assess its long-term stability. Field observations and ring shear tests revealed that the landslide exhibited high mobility in both the source area and along its movement path. Following field investigations and laboratory experiments, Wang et al. [39] concluded that the excess pore water pressure, generated by particle fragmentation, reduced shear resistance during movement, making it a key factor in the landslide's high mobility, as illustrated in Figure 3.

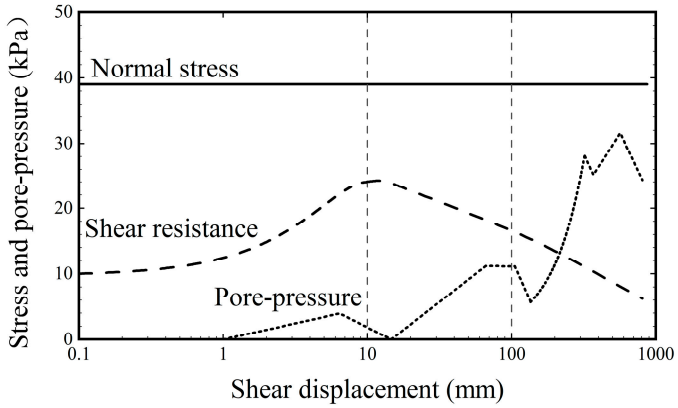



**Figure 3.** Stress and pore pressure induced by particle fragmentation against shear displacement (data source from Wang et al. [39]).

Locat et al. [2] suggested that particle fragmentation consumes energy, thereby reducing kinetic energy and mobility. However, fragmentation and grinding mechanisms increase the volume of fine materials (e.g., fine sand, silt, and clay), especially in the basal shear zone. This reduction in pore space, when water is present, leads to elevated pore water pressure within or at the base of the moving mass, facilitating material flow and enhancing mobility. In subsequent research, Locat et al. [2] analyzed nine long-runout landslides from the European Alps and Canadian Rockies, identifying a significant positive correlation between the extent of particle fragmentation and landslide volume. Consequently, Locat et al. [2] found that potential energy per unit volume normalized by rock strength is strongly correlated with the degree of particle fragmentation, as illustrated in Figure 4, which may suggest that a landslide with a greater degree of particle fragmentation has a higher potential energy per unit volume to enhance its mobility.

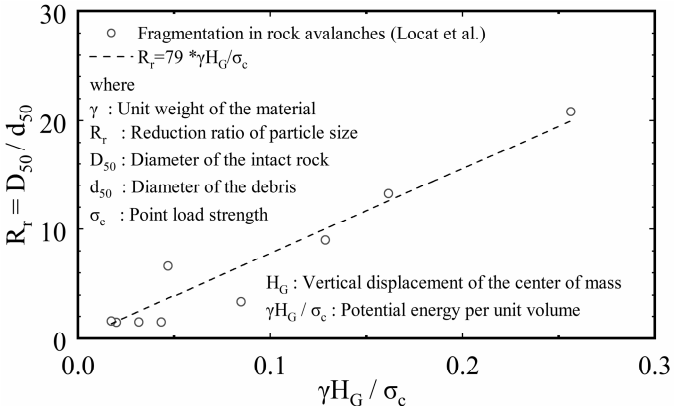



**Figure 4.** Degree of particle fragmentation against rock-strength-normalized potential energy per unit volume (data source from Locat et al. [2]).

Bowman et al. [24] conducted a series of physical modeling experiments on rock avalanche behavior using a geotechnical centrifuge with coal on a sloped chute to investigate the effect of particle fragmentation on the extraordinarily long runout distances observed in long-runout landslides. A positive correlation was revealed between the runout distance and relative breakage ($B_r$) of landslides, demonstrating that the increase in particle fragmentation results in a longer runout distance, as illustrated in Figure 5. Additionally, the experiments revealed that particle fragmentation not only leads to more dispersed deposits but also causes a shift in the mass center of the deposits.

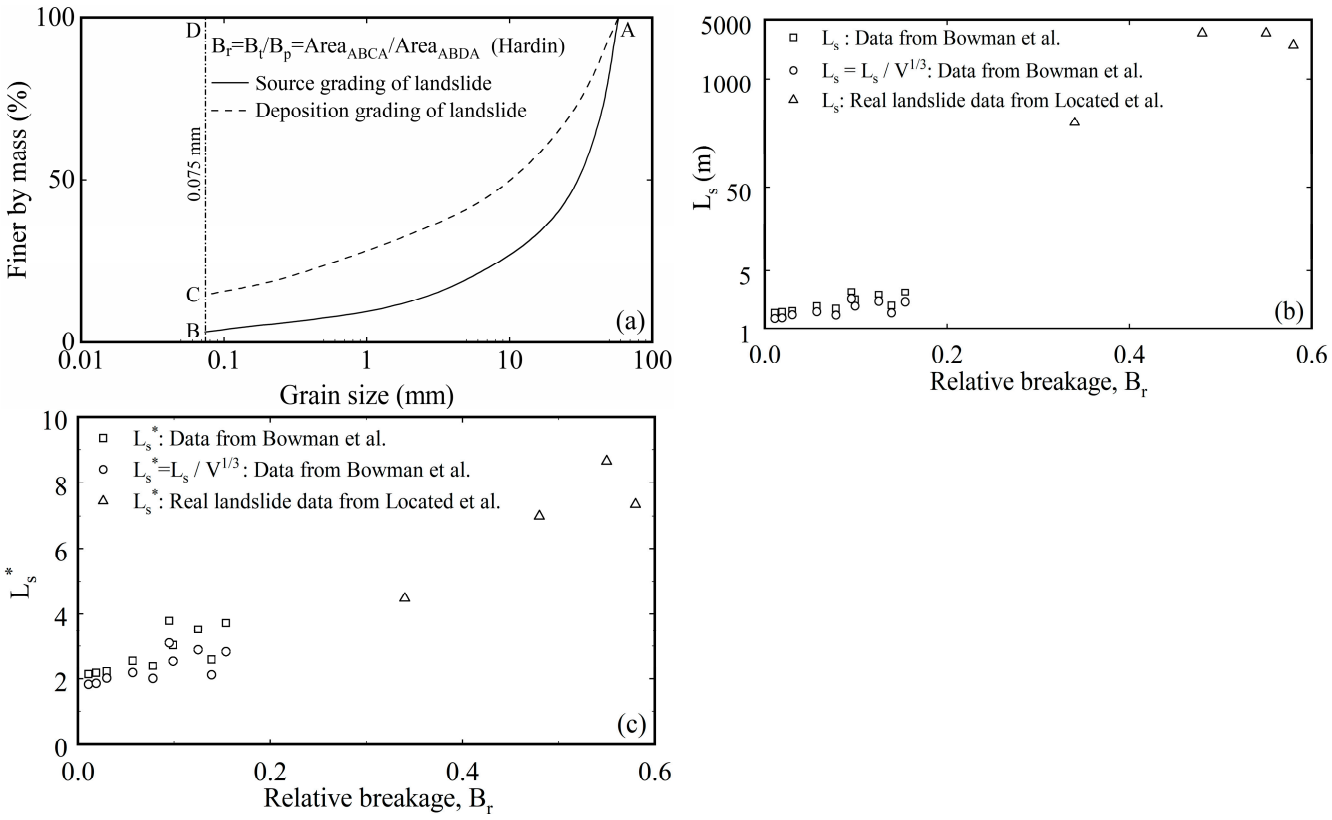



**Figure 5.** Relative breakage and runout distance of landslides: (**a**) the definition of the relative breakage ($B_r$) by using the gradings before and after particle fragmentation (adopted from Hardin [25]); (**b**) runout distance $L_s$ against relative breakage; (**c**) normalized runout distance ($L_S^* = L_S/V^{1/3}$) against relative breakage (data source from Bowman et al. [24] and Locat et al. [2]).

Hu et al. [32] conducted a number of rotary shear experiments on crushable materials (quartz, dolomite, fluorite, and rock salt) using a high-speed rotary shear apparatus to investigate the weakening rheology of dry granular flow incorporating particle fragmentation, where the granular materials show weaker and less shear resistance during a prolonged rapid shear and the potential mechanism of particle fragmentation may greatly reduce the subsequent shear resistance due to the thixotropy.

Despite the presence of contradictory evidence concerning the impact of particle fragmentation on the mobility of high-speed long-runout landslides (as fragmentation has been shown to reduce overall energy [2]), extensive laboratory experiments in conjunction with field investigations have confirmed that particle fragmentation significantly increases landslide mobility [2,22–24,31–33,39]. In the future, it is anticipated that new experiments—such as those examining the combined effects of particle fragmentation and fluid media on landslide behavior—will provide stronger evidence that particle fragmentation significantly enhances flowability.

### *3.2. Role of Dynamic Grain Segregation on Mobility of Long-Runout Landslides*

Grain segregation is also a key process in long-runout landslides [28–30,40]. A number of studies reveal that the granular structure of reverse grading, a typical characteristic of the dynamic behavior of long-runout landslides, is formed through the process of grain mixing and segregation [7,22,27–30], as illustrated in Figure 6.

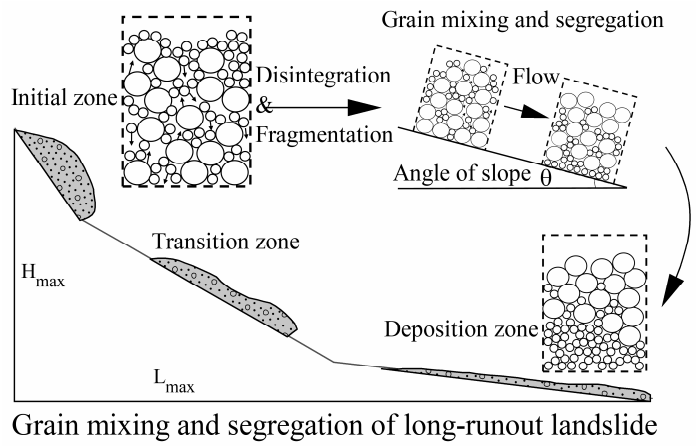



**Figure 6.** Illustration of grain mixing and segregation of long-runout landslide.

Few studies have shown that segregation during the movement of landslides also plays a crucial role in the mobility of long-runout landslides [30,31,41–44]. For example, using discrete element numerical simulation, Zhou et al. [41] demonstrated that grain segregation at the front edge of the sliding mass can significantly affect both the mobility and flow state of the sliding front. Similarly, physical model experiments by Kokelaar et al. [42] revealed that particle segregation at the leading edge promotes lubrication of the sliding surface, which in turn results in an increased sliding distance.

Zhou et al. [43] found that grain segregation in debris flow causes the rearrangement of pore pressures within the particle mass as a means of affecting the behavior of debris flow, e.g., the velocity of the flow front, the length of the particle mass, the internal shear rate, and the energy transport paths within the mass, which enhances the mobility of the debris flow by slowing down the energy dissipation during the motion.

Li et al. [44] employed the three-dimensional discrete element method, combined with model test results, to investigate the influence of grain segregation on the mobility of the sliding mass. Experiments were conducted with single-size particles and mixed-size particles on a chute with the same slope. The results showed that, under varying characteristic particle size conditions, grain segregation in the mixed-size particle mass led to higher mobility and faster movement.

John [30] found that once particles are vertically segregated into a reverse-graded layer (where large particles are on top of smaller ones), deep shear causes large particles to preferentially move towards the flow front, where they can be overthrown, resegregated, recirculated, and accumulated. As a result, gravity-driven segregation can lead to secondary lateral segregation. This segregation, combined with differences in friction or particle shape, can create a strong feedback effect on the overall flow. Larger particles tend to accumulate at the flow front, and if their friction exceeds that of smaller particles, it can further influence the flow, leading to longer distances and increased mobility.

Yu and Su [31] conducted an experimental investigation into the mobility characteristics of dry granular flow, by a number of flume tests on silica sand to interpret the effect of granular structure on the mobility of landslides, showing a great effect of the initial structure of granular material on the mobility of granular flow.

### *3.3. Role of Air on Mobility of Long-Runout Landslides*

Kent [45] and Shreve et al. [46] were among the first to suggest the influence of air on long-runout landslides. After reviewing numerous landslides worldwide, Kent [45] concluded that during the shearing and falling of the landslide mass, a significant quantity of air was entrapped between the bottom of the sliding mass and the ground. When the

landslide collided with the mountain and fractured, the particles at the bottom of the debris flow mixed with the trapped air, forming a "fluidized bed." The interaction between the gas and solid particles replaced inter-particle collisions as the primary means of force transmission. As a result, the ground friction resistance experienced by the debris flow was nearly zero, allowing the debris flow to move at high speed. Shreve et al. [46], building on Kent's research, argued that air fluidization occurs not only at the base of the landslide but throughout the entire mass.

By comparing volcanic landslides with other types, Cheng et al. [6] found that volcanic debris flow moves faster due to the strong involvement of gases, which fluidize the flow and increase its mobility. Particularly in the numerous landslides triggered by the 2008 Wenchuan earthquake, the terrain effectively trapped air, allowing it to fluidize the debris flow and greatly enhance the mobility of landslides [20,47–50]; e.g., in the Wenjiagou landslide, the dry debris flow at the top of the sliding mass compressed trapped air in the hook-shaped valley at two turning points, creating a noticeable "air cushion effect" [20].

However, the role of air in fluidizing long-runout landslides has been met with considerable skepticism, particularly with advancements in research on extraterrestrial landslides [1,7]. The air fluidization hypothesis fails to explain the occurrence of long-runout landslides in extraterrestrial environments where air is absent. Furthermore, the mechanisms by which air could be entrapped and remain within the moving landslide mass remain unclear [1,5,7,8]. Consequently, while the hypothesis that air reduces the basal shear strength cannot be discounted, it is improbable that air is the primary cause of the high mobility of long-runout landslides.

### *3.4. Role of Water on Mobility of Landslides*

Water plays a significant role in the mobility of long-runout landslides, as demonstrated in various studies [1,7,39,51–53]. Water reduces particle friction through the development of high pore pressure, similar to the dynamics of saturated debris flows [51]. However, landslides, typically at the bottom, become saturated with water, potentially meaning that water can also enhance the mobility of landslides [1,54,55]. Initially, landslides may form as solid–gas two-phase debris flows, but when water is incorporated, they transition into three-phase wet debris flows, which possess high kinetic and potential energy, leading to extremely destructive impacts [6,54,55]. Furthermore, the model of excess pore water pressure at the base of a landslide, proposed by Professor Sassa of Japan and his colleagues, is another important factor explaining how water enhances the mobility of long-runout landslide flows [39,51].

However, in the case of large catastrophic rock avalanches, the available amount of water is typically insufficient to saturate most of the moving material; this theory cannot explain the occurrence of long-runout landslides in dry (unsaturated) granular flows [7]. Therefore, the conditions under which water significantly enhances the mobility of long-runout landslides are stringent [7,8].

### *3.5. Role of Ambient Settings on Mobility of Long-Runout Landslides*

#### 3.5.1. Role of Extraterrestrial Settings on Mobility of Long-Runout Landslides

Since the 1980s, with the advancement of human exploration technologies for extraterrestrial planets, the study of extraterrestrial landslides has emerged as a new trend [1,7,56,57]. Even in the thin atmosphere and low-water conditions of outer space, long-runout landslide flows remain highly active [1,57]. This area of research offers novel perspectives that challenge our existing theoretical frameworks [1,3,54–59].

Following the compilation of a substantial dataset, researchers found that long-runout landslides on Mars are not only substantial in volume but also highly mobile [3,54,55,57,58].

Initially, it was assumed that Martian long-runout landslides would have low mobility due to the lack of fluids. However, subsequent studies have revealed that the melting of surface ice at the shallow surface of the planet caused by the occurrence of Martian landslides, as well as the clays and minerals at the base of landslides, both play a role in fluid lubrication, which allows Martian landslides to remain highly mobile [1,58]. Moreover, research on Martian landslides has shown that many of these landslides occur in well-defined terrain, and after impact events, the ice within the landslide voids melts in large quantities or is replaced by other fluid materials, further enhancing the mobility of the landslides [57].

Comparative studies of Martian and terrestrial landslides, based on numerical simulations by Johnson et al. [59] and Yu et al. [55], have found that gravity has little effect on landslide mobility when fluids are not considered. This suggests that processes observed in dry granular flows could help explain the hypermobility of long-runout landslides on Earth, Mars, and potentially other celestial bodies, such as Iapetus.

Research on landslides on Mars is of significant importance for the understanding of the long-runout landslides. As demonstrated in Figure 2, the long-runout landslides occurring on Mars are characterized by both substantial volume and remarkably high mobility. A thorough analysis of these phenomena indicates that air may not be an indispensable factor in influencing landslide behavior. However, extensive studies indicate that the fluidity of Martian landslide flows remains profoundly impacted by air [1,55,57,58]. Moreover, energy transfer models have been developed [59]. Future research on extraterrestrial landslides has the potential to elucidate the enigma of the exceptional mobility observed in the long-runout landslides.

#### 3.5.2. Role of Submarine Settings on Mobility of Long-Runout Landslides

Recent studies have identified the phenomenon of submarine landslides as a subject of research interest, alongside the study of extraterrestrial landslides [1,55,60–63]. Unlike Martian landslides, submarine landslides typically have much higher mobility with a minimum H/L value of 0.004 in the Appendix to generate extremely high speeds compared to subaerial landslides [1,61,62]. Earlier research indicated that landslides containing a certain amount of water would convert into debris flows [64]. However, further research surprisingly revealed that the mobility of most submarine landslides is far lower than that of debris flows, and more similar to landslides, with deposition characteristics resembling those of subaerial landslides [1,60,65]. Furthermore, the high mobility of submarine landslides is hypothesized to be possibly related to elevated pore water pressure [1,61–63]. And the greater speed of submarine landslides is caused by the large amount of water mixing in to create low viscosity, highly mobile turbidity currents [7,62,63].

As exploration technology has advanced, research on extraterrestrial and submarine landslides has significantly enhanced current understanding of the hypermobility of long-runout landslides, e.g., the substantial volume and remarkably high mobility of the long-runout landslides on Mars may be associated with impacts, whereby a proportion of the impact energy is directly transferred to the slope material, resulting in its destabilization and subsequent flow down the slope [57]. Additionally, considering the extreme mobility of submarine landslides, it is reasonable to expect that long-runout landslides triggered by heavy rain or in glacial regions could exhibit far greater mobility and destructiveness than previously thought. However, there is still a long way to go to uncover the mystery of the long-runout landslide.

## 4. Dynamic Process of Long-Runout Landslides

The typical process of long-runout landslides can usually be divided into the initiation process, the transition process, and the deposition process, which are herein summarized

and described by incorporating the general movement process and formation mechanisms of long-runout landslides.

### 4.1. Initial Process of Long-Runout Landslides

Landslide initiation is the process of overall or localized sliding along a weak or shear surface of a slope rock and soil body when affected by external factors (e.g., rainfall, earthquakes, groundwater activity, human activities, etc.). The initiation stage of long-runout landslides occurs in the source area, and the main mechanisms influencing landslide initiation include the following:

(1) Intense rainfall: Long-runout landslides such as the Shuicheng landslide, the Zhaojiagou landslide, the Sucun landslide, and the Heggeis landslide were all caused by intense rainfall [4,39,52,53]. Rainwater infiltration triggers a series of hydrological responses in the slope and alters the stress state of the rock and soil mass [4]. On the one hand, rainwater infiltration increases the mass of the slope, thereby intensifying the downslope driving force. On the other hand, rainfall reduces the matric suction in unsaturated soils, leading to the generation of positive pore water pressure to impair the effective stress and shear resistance, ultimately causing landslide initiation [66]. Similarly, heavy rainfall usually leads to infiltration to form perched water, causing slope failure (landslide occurrence) at a critical point by raising pore water pressure to reduce shear strength of slope [67].

(2) Earthquakes: Landslides triggered by the Wenchuan earthquake and the Kashmir earthquake are given herein as examples of earthquake-induced long-runout landslides [15,20,47,68]. Strong earthquakes usually fracture mountain peaks, causing rock masses on the upper slopes to be ejected downward, while also triggering the rapid, oblique sliding of stratified rock layers on steep slopes, leading to the initiation of landslides [47]. In addition, under the cyclic loading of seismic waves, since the landslide source area is near the earthquake epicenter, the time difference between the arrival of seismic P-waves and S-waves is minimal. As a result, the forces acting on the slope take the form of periodic tensile, compressive, and shear coupled inertial forces, causing tensile failure in the original slope and initiating the landslide [20].

(3) Erosion by water or human activities: In recent years, some long-runout landslides have been triggered by river erosion or human activities [48,68,69], e.g., the Jiweishan landslide occurred under unfavorable geological conditions, exacerbated by long-term gravitational pressure, karst activity, and human activities such as mining. The event occurred when the key block, which was acting as a barrier, was sheared off to lead to a large scale landslide [68]. One of the causes of the Luojiapo landslide was the local rise in groundwater levels, which, combined with water erosion, compromised the slope's stability, eventually causing the landslide [69].

When a landslide is triggered by heavy rainfall, earthquakes, long-term water erosion, or human activities, during the initiation process, the landslide typically moves slowly, with friction being the dominant interaction between particles. After the initiation process of a landslide, the landslide moves into the next process, i.e., the transition process.

### 4.2. Transition Process of Long-Runout Landslides

Once the initiation of a landslide ends, a long-runout landslide usually moves into a transition process, including the sustained acceleration and deceleration processes [70]. During this stage of a landslide, gravitational potential energy is quickly transformed into kinetic energy [4,20,53,69–71]. This stage typically takes place in the early to middle section of the landslide's transition process. A portion of the landslide may enter the flying or ejecting state (e.g., DaGuangbao landslide) while the speed of the landslide significantly

increases in this stage [4,53]. As it passes through the erosion zone, the complex, uneven terrain is often accompanied by mud or water as well as the potential for effective trapping of air (e.g., the Wenchuan earthquake triggered landslides) and the occurrence of extensive particle fragmentation and grain segregation, which greatly increases the mobility of landslides [2,4,20,38,44]. During this stage, the landslide accelerates extremely quickly, with maximum speeds reaching over 200 m/s [7,26]. Landslide speeds generally reach their peak during this stage. Following the end of the sustained acceleration phase, the landslide transitions into the sustained deceleration stage. This stage generally occurs in the latter part of the transition process [44,72,73]. During this stage, the terrain becomes gentler, and dynamic friction generated by erosion comes into play [4]. Moreover, at this stage, the influence of air or water is expelled as it percolates out. Effective stress is replaced by granular soil particles, e.g., friction increases sharply, and the landslide's shear strength rises, where the landslide's "fluidization" effect nearly disappears, causing a transformation into a sustained deceleration process of the landslide.

### *4.3. Deposition Process of Long-Runout Landslides*

As a landslide's speed continues to decrease, stagnation and extensive deposition occur, during the stage of which the landslide's kinetic energy is exhausted to undergo an extensive deposition. However, throughout the entire movement process of a landslide, deposition occurs alongside motion, which explains why the deposition length and area of long-runout landslides are so extensive.

## 5. Dynamic Mechanisms and Models for Long-Runout Landslides

Long-runout landslides, as listed in the Appendix, usually cause immeasurable damage in life and property. Consequently, unraveling the mystery of long-runout nature has become a focal point of research. In order to understand the dynamic mechanisms of long-runout landslides, a number of models have been proposed, e.g., the air lubrication model [6,7,44,45,74,75], granular flow model [5,74–77], energy transfer model [23,78,79], acoustic fluidization model [80,81], excess pore water pressure model [39,51,77], flash heating model [3,82–88], and rheological model [9,32,89–94], which are briefly summarized in this section, including the details of two widely recognized dynamic models: the flash heating model and the rheological model.

### *5.1. Early Models for Long-Runout Landslides*

Before the rise in flash heat models and rheological models, many other models had been used with the purpose of unearthing the mystery of long-runout landslides [5,45,46,51,74–81,95]. In detail, the air fluidization model suggests that during a landslide's shearing and fall, a large amount of air becomes trapped between the sliding mass and the ground [5,45,46]. When it collides with the mountain and breaks apart, the bottom particles of landslides mix thoroughly with the trapped air to form a "fluidized bed" as a cushion to support the landslide, where the interaction between air and particles replaces inter-particle collisions as the primary mode of force transmission. However, once the air escapes due to infiltration, friction increases dramatically, and the movement of the landslide slows or ceases [5–7,45,46,75]. While the model explains some aspects of landslide behavior, it struggles to explain the sustained movement of long-runout landslides in environments with high air permeability or landslides that occur outside of terrestrial environments [1,5,7,75].

The granular flow model posits that collisions among particles in granular flows contribute to their long-runout movement [5,74,76]. As velocity increases, the friction angle of dry granular materials undergoing rapid shear decreases due to dynamic interactions,

causing particles to push apart [74,76]. During motion, the shear stress from the ground becomes significant enough for the bottom particles to exert upward forces on the upper particles, leading to an expansion of the granular flow. This expansion brings in fluid (often dust), reducing the effective stresses among the granular particles and the ground surface, which results in a decrease in frictional resistance. Consequently, the landslide can move at high speeds and over long distances [5,7,74,76,94]. However, the granular flow model cannot explain the "size effect" of long-runout landslides, nor can it fully account for the reduction in kinetic friction during debris flow motion [5,7,77].

In addition, the energy transfer model suggests that energy transfer plays a key role throughout the movement of the landslide [5,23,78,79]. The granular particles of a landslide are subjected to shear stress from the surrounding environment while the landslide moves at high speed. And, when the shear stress exceeds the shear strength of the particles, they break apart, with some stopping and transferring their kinetic energy to others. The particles receiving this energy will move forward by keeping a high speed to flow in long-runout distance [5,7,23,26,78,79]. In addition to the above models, there are also others, e.g., the acoustic fluidization model [5,80–82] and the excess pore water pressure model [39,51,75], which have also made some outstanding contributions to understanding the mechanisms of the long-runout landslides, and will not be elaborated here.

### 5.2. Flash Heating Model for Long-Runout Landslides

The precursor to the flash heating model was a qualitative model proposed by Heaton [82] based on earthquake fault studies, which was mainly characterized by the assumption that the friction on the fault surface was inversely proportional to the local slip velocity because of the thermal effect. Tsutsum [83] employed a rotary shear high-speed friction apparatus to conduct friction tests on a pair of hollow cylindrical gabbro samples, firstly demonstrating the feasibility of the model in real materials. The original flash heating model was developed from this foundation.

In recent years, by following the studies on the flash heating model, it may be one of the main causes of the frictional weakening in long-runout landslides [3,84–88]; e.g., laboratory tests on flash heating models have indicated that the flash heating due to frictional heating thermally pressurizes landslide pore fluids to reduce the equivalent friction coefficient by maintaining high pore pressures for a longer period of time [84,85]. Furthermore, experiments at sufficiently high slip rates have shown that the heat generated at the block contact does not have enough time to diffuse appreciably, leading to an increase in contact temperature and a decrease in contact strength. Consequently, high contact stresses and high slip rates may cause transient heating, or even melting of the contact, causing a low shear strength and low friction [3,9,32,86,87].

Based on an earlier concept, a basic flash weakening model was given to quantify the steady state friction coefficient as a function of sliding velocity, as expressed by

$$\mu(U) = \begin{cases} (\mu_o - \mu_w)/(\|U\|/U_w) + \mu_w & \|U\| > U_w \\ \mu_o & \|U\| \leqq U_w \end{cases} \quad (1)$$

where $\mu(U)$ is the friction coefficient related to $U$ that is the sliding velocity, $U_w$ is the characteristic velocity at the onset of rapid weakening, $\mu_o$ is the static friction coefficient, and $\mu_w$ is the thermally weakened friction coefficient. By combining the concepts of the flash heating law and rheological law, a multiscale friction law for granular flow was proposed by Lucas et al. [3] to explain the velocity weakening mechanism of long-runout landslides:

$$\mu(U) = (\mu_o - \mu_w)/(1 + \|U\|/U_w) + \mu_w \quad (2)$$

In recent years, the flash heating model on long-runout landslides has remained a cutting-edge research focus; e.g., a multi block thermal pore pressure model was employed to interpret the effect of friction weakening induced by thermal pore pressure on the hypermobility of long-runout landslides [88]. However, the model exhibits certain deficiencies, e.g., the granular material composition and velocity characteristics of high-speed long-runout landslides are exceedingly intricate, which poses significant challenges to data collection. Velocity parameters at different stages of landslide motion vary with flow depth and are also difficult to measure. Furthermore, the effects of particle fragmentation and the particle segregation characteristics of high-speed long-runout landslides cannot be adequately characterized. In the future, more coupled studies are anticipated in integrating numerical simulations, laboratory experiments, and field data; e.g., incorporating real time monitoring of temperature and pressure changes at the landslide base into numerical simulations, then combining these with laboratory experiments and field data, will further validate and refine the flash heat model.

### *5.3. Rheological Model for Long-Runout Landslides*

In addition to the flash heating model, the rheological model is also of critical importance in understanding the dynamic mechanisms of long-runout landslides, by virtue of its ability to follow the behavior of granular flow [3,9,31,89–94].

Through extensive experiments and numerical simulations, the researchers classified the dry granular flow into three regimes: a slow strain rate (or quasi-static) regime with friction-like flow behavior; an intermediate strain rate (or elastic-inertial) regime having relatively densely packed particles with a high enough shear rate to cause transient contact networks; and a high strain rate (or rapid kinetic inertial-collisional) regime with relatively dilute conditions characterized by binary particle interactions [3,9,32,89–94]. And the dynamic model that describes the dry granular flow model is called a rheological model.

Studies from numerical simulations and experiments have shown that, for stiff particles, the shear stress $\tau$ is proportional to the normal stress $P$, with a coefficient of proportionality function of a single dimensionless number—inertial number $I$ [3,32,89–92], as given below:

$$\mu(I) = \tau / P \; with \; I = \dot{\gamma} d / \sqrt{P/\rho_s} \tag{3}$$

where $\mu(I)$ is the friction coefficient related to inertial number $I$, $\dot{\gamma}$ is the shear strain rate, $d$ is the particle diameter, $P$ is the normal stress and $\rho_s$ is the granular flow density. As $I$ increases, $\mu$ increases with $I$ until it reaches a threshold, after which it decreases [89].

Cruz et al. [90] revealed that the shear state is also governed by the inertial number $I$. As $I$ increases in a medium density state (similar to fluid flow), Cruz et al. [91] observed an approximately linear decrease in solid fraction from the maximum packing value. The effective friction coefficient increased approximately linearly from the static internal friction value. A corresponding $\mu(I)$ model is proposed as

$$\mu(I) = \mu_o + bI \tag{4}$$

where $\mu(I)$ is the friction coefficient related to inertial number $I$, $\mu_o$ is the quasi-static coefficient of friction, and $b$ is the linear coefficient value.

In addition, Cruz et al. [90] found that $\mu_o$ and $b$ depend on physical and mechanical particle parameters such as the restitution coefficient $e$. In follow up research, Cruz et al. [90] suggested that when $I \approx 10^{-1}$, there is a transition from dense granular flow to a collisional regime. This causes the effective friction strength to rapidly increase and reach saturation in a fully collisional state.

After conducting further experimental simulations, a more general friction law is proposed by Jop et al. [91], in Figure 7, as expressed below:

$$\mu(I) = \mu_s + (\mu_2 - \mu_s)/(I_0/I + 1) \tag{5}$$

where $\mu(I)$ is the friction coefficient, $\mu_s$ is the quasi-static friction coefficient ($I < 10^{-3}$), $\mu_2$ is the limiting value of the effective friction coefficient that converges at high shear rates (when $I$ is large), $I_0$ is a constant inertial number, and $I$ is the inertial number. In simulation studies using discrete element methods, Hatano's numerical simulations revealed that when the inertia number $I$ is small (greater than or equal to $10^{-4}$), as illustrated in Figure 7, the model displays power-law behavior [92] as

$$\mu(I) = \mu_s + \alpha I^n \tag{6}$$

where $\mu(I)$ is the friction coefficient related to the inertial number $I$, $\mu_s$ is the quasi-static coefficient of friction, and $\alpha$ and $n$ are material constants. In fact, the rheological behavior of granular flow was greatly affected by the physio-mechanical properties of granular materials [92–94]; e.g., breakage enhances the mobility of granular flow by decreasing its friction coefficient [93].

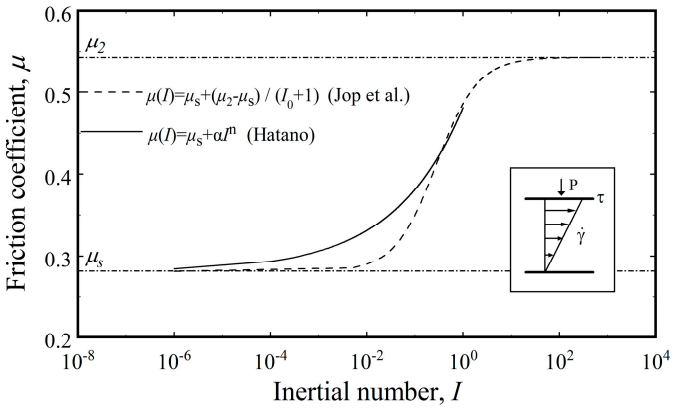



**Figure 7.** Relation of friction coefficient $\mu$ and inertial number $I$ of granular flow (Data source from Jop et al. [90] and Hatano [91]).

As computer technology advances and numerical simulations become more prevalent, the rheological model of granular flow has increasingly become a focus of cutting-edge scientific research. For example, some experimental results using the coupling of flume and rheological modeling show that the flow characteristics of granular flow are related to particle size and volume, and as particle size decreases and volume increases, the overall shear rate decreases, leading to a decrease in the equivalent friction angle and an increase in granular flow [9,31]. In addition, the study of particle flow has further enriched the study of entrainment-induced liquefaction in long-runout landslides [94]. However, the rheological model also has its limitations, e.g., the model is derived from numerical experiments with monodispersed particles and cannot be adapted to high-speed long-runout landslides with polydisperse particle systems with particle fragmentation and particle segregation. In fact, the extension of rheological models is expected to encompass the complexity of natural landslide materials. This requires experiments and simulations involving polydisperse particle systems to gain a deeper understanding of how friction and flow characteristics are influenced by particle size, segregation, particle shape, and material diversity.

## 6. Conclusions

A great number of past studies on long-runout landslides, both nationally and internationally, have seen a surge in a range of innovative ideas and vigorous debates contributing to the advancement of understanding the phenomenon and mechanism of the hypermobility of long-runout landslides. However, the dynamic mechanisms of long-runout landslides remain unresolved, continuing to attract the great interest of geoscientists in the expectation of uncovering the mystery of the hypermobility of long-runout landslides. In this paper, a review on the dynamics of long-runout landslides was comprehensively summarized, as briefly concluded below.

(1) A long-runout landslide is recognized as a wide geophysical process in nature, being usually characterized by its hypermobility ($H_{max}/L_{max}$ is rather lower than 0.6). In fact, long-runout landslides are always associated with their process of disintegration and fragmentation to yield the process of grain mixing and segregation, causing extremely complicated dynamics of long-runout landslides, especially involving the pore fluids, e.g., air, water.

(2) Mobility of long-runout landslides is greatly affected by the disintegration and fragmentation, grain segregation, and pore fluids (i.e., air, water) and ambient settings (i.e., extraterrestrial and submarine settings). The fragmentation and high-speed shearing of granular material in long-runout landslides may enhance the mobility of landslides by decreasing the friction resistance. In addition, grain segregation and pore fluids (i.e., air, water) also play a great role in affecting the mobility of long-runout landslides, e.g., in some special reality, the increase in pore water pressure caused by particle fragmentation plays a great role in decreasing the shear resistance to enhance the mobility of landslides. In fact, ambient settings of landslides are of significance to affect their mobility, e.g., submarine landslides are always hypermobile. In the future, a combination of experimental numerical simulations and field investigations will be employed to study the coupled effects of particle fragmentation, particle segregation, fluid media, and environmental factors on the dynamics of long-runout landslides. This approach will provide a more comprehensive explanation for the hypermobility observed in long-runout landslides.

(3) In addition to mobility, the dynamic process of long-runout landslides is reviewed, as summarized by the initial process, transition process, and deposition process of landslides, being greatly affected by the disintegration and fragmentation and the grain mixing and segregation of landslides. The initial process of a landslide is a gravity-driven process that is usually caused by intense rainfall, earthquakes, and erosion by water or human activities. In the transition process of a long-runout landslide, the disintegration and fragmentation, grain mixing and segregation, and the possible involvement of fluid media, e.g., air, water, contribute to its hypermobility. However, the deposition process of long-runout landslides shows the process of landslides to stagnation as the kinetic energy is exhausted to undergo an extensive deposition.

(4) In terms of the dynamic models of long-runout landslides, some models are summarized here, e.g., the air fluidization model, granular flow model, energy transfer model, flash heating model, and rheological model, showing great roles in understanding the dynamics of long-runout landslides.

In fact, however, the advances of the past studies on long-runout landslides are still insufficient to fully capture the complex behavior of long-runout landslides, e.g., the mechanisms underlying the disintegration and fragmentation and grain mixing and segregation incorporating the effects of pore fluids, and the related dynamic behavior and models. In the future, addressing these gaps will become a theme of global focus on uncovering the origin and nature of the dynamics of long-runout landslides.

**Funding:** This work was supported by the Sichuan Science and Technology Program—China (Grant no. 2023ZYD0149), National Natural Science Foundation of China (Grant no. U22A20603) and CAS "Light of West China" Program—China (Grant no. Fangwei Yu).

**Conflicts of Interest:** The authors declare no conflict of interest.

## Appendix A

**Table A1.** Data of 284 long-runout landslides.

| Landslides | $H_{max}/L_{max}$ | Volume $V$ (km$^3$) | Area $A$ (km$^2$) | $H_{max}$ | $L_{max}$ | Types of Landslides | References |
|---|---|---|---|---|---|---|---|
| Saidmarreh | 0.321 | 21 | / | 4800 | 15,000 | Subaerical landslides | [96] |
| Martinez | 0.246 | 0.38 | / | 1877 | 7600 | Subaerical landslides | [97] |
| Nevados Huascarán | 0.25 | 50~100 | 22.5 | 4000 | 16,000 | Subaerical landslides | [14] |
| Rubble Creek | 0.230 | 0.025 | / | 1060 | 4600 | Subaerical landslides | [98] |
| Bualtar I | 0.404 | 0.01 | / | 1940 | 4800 | Subaerical landslides | [22] |
| Bualtar II | 0.386 | 0.007 | / | 1430 | 3700 | Subaerical landslides | [22] |
| Bualtar III | 0.541 | 0.003 | / | 1300 | 2400 | Subaerical landslides | [22] |
| Pandemonium Creek | 0.222 | 0.005 | / | 2000 | 9000 | Subaerical landslides | [99] |
| Blackhawk | 0.125 | 0.28 | / | 1200 | 9600 | Subaerical landslides | [100] |
| Corno di desde | 0.324 | 0.02 | / | 1200 | 3700 | Subaerical landslides | [100] |
| Deyen, Glarus | 0.112 | 0.6 | / | 740 | 6600 | Subaerical landslides | [100] |
| Diablerets | 0.345 | 0.05 | / | 1900 | 5500 | Subaerical landslides | [100] |
| Disentis | 0.352 | 0.015 | / | 740 | 2100 | Subaerical landslides | [100] |
| Elm | 0.308 | 0.01 | / | 710 | 2300 | Subaerical landslides | [100] |
| Engelberg | 0.216 | 2.75 | / | 1600 | 7400 | Subaerical landslides | [100] |
| Fernpass | 0.089 | 1 | / | 1400 | 15,600 | Subaerical landslides | [100] |
| Flims | 0.128 | 12 | / | 2000 | 15,600 | Subaerical landslides | [100] |
| Frank | 0.248 | 0.03 | / | 870 | 3500 | Subaerical landslides | [100] |
| Garnish | 0.253 | 0.8 | / | 1900 | 7500 | Subaerical landslides | [100] |
| Goldau | 0.200 | 0.035 | / | 1200 | 6000 | Subaerical landslides | [100] |
| Gros Ventre | 0.164 | 0.038 | / | 560 | 3400 | Subaerical landslides | [100] |
| Kandertal | 0.191 | 0.14 | / | 1900 | 9900 | Subaerical landslides | [100] |
| Maligne Lake | 0.168 | 0.5 | / | 920 | 5470 | Subaerical landslides | [100] |
| Medicine Lake | 0.262 | 0.086 | / | 320 | 1220 | Subaerical landslides | [100] |
| Madison | 0.268 | 0.029 | / | 430 | 1600 | Subaerical landslides | [100] |
| Mombiel | 0.462 | 0.0008 | / | 370 | 800 | Subaerical landslides | [100] |
| Obersee GL | 0.360 | 0.12 | / | 1800 | 5000 | Subaerical landslides | [100] |
| Pamir | 0.241 | 2 | / | 1500 | 6200 | Subaerical landslides | [100] |
| Poshivo | 0.365 | 0.15 | / | 1500 | 4100 | Subaerical landslides | [100] |
| Saidmarreh | 0.079 | 20 | / | 1500 | 18,900 | Subaerical landslides | [100] |
| Schachental | 0.580 | 0.0005 | / | 1800 | 3100 | Subaerical landslides | [100] |
| Scimada Saoseo | 0.272 | 0.08 | / | 1500 | 5500 | Subaerical landslides | [100] |
| Sherman | 0.209 | 0.03 | / | 1300 | 6200 | Subaerical landslides | [100] |
| Siders | 0.137 | 1.5 | / | 2400 | 17,400 | Subaerical landslides | [100] |
| Tamins | 0.096 | 1.3 | / | 1300 | 13,500 | Subaerical landslides | [100] |
| Vaiont | 0.333 | 0.25 | / | 500 | 1500 | Subaerical landslides | [100] |
| Val Lagone | 0.418 | 0.00065 | / | 1005 | 2400 | Subaerical landslides | [100] |
| Voralpsee | 0.323 | 0.03 | / | 1100 | 3400 | Subaerical landslides | [100] |
| Wengen 1 | 0.454 | 0.0025 | / | 500 | 1100 | Subaerical landslides | [100] |
| Wengen 2 | 0.421 | 0.0055 | / | 590 | 1400 | Subaerical landslides | [100] |
| Tsergo ri | 0.0505 | 10 | / | 3030 | 60,000 | Subaerical landslides | [100] |
| Valpola | 0.2 | 0.34 | / | 800 | 4000 | Subaerical landslides | [101] |
| Ontake | 0.12 | 0.036 | / | 1550 | 12,000 | Subaerical landslides | [102–104] |
| Dusty Creek (1963) | 0.416 | 0.005 | / | 1000 | 2400 | Subaerical landslides | [105] |
| Dusty Creek (1984) | 0.5 | / | / | 1000 | 2000 | Subaerical landslides | [106] |
| Usoi | / | 0.5 | / | 1800 | / | Subaerical landslides | [107] |
| Slide Mountain | 0.254 | 0.013 | / | 420 | 1650 | Subaerical landslides | [2] |
| Queen Elization | 0.3591 | 0.045 | / | 950 | 2645 | Subaerical landslides | [2] |

**Table A1.** *Cont.*

| Landslides | $H_{max}/L_{max}$ | Volume $V$ (km$^3$) | Area $A$ (km$^2$) | $H_{max}$ | $L_{max}$ | Types of Landslides | References |
|---|---|---|---|---|---|---|---|
| Johas Creek North | 0.307 | 0.00024 | / | 860 | 2800 | Subaerical landslides | [2] |
| Johas Creek South | 0.466 | 0.00049 | / | 900 | 1830 | Subaerical landslides | [2] |
| Claps de Luc | 0.462 | 0.0002 | / | 370 | 800 | Subaerical landslides | [2] |
| LA Madeleine | 0.277 | 0.09 | / | 1250 | 4500 | Subaerical landslides | [2] |
| Khait | 0.191 | 0.75 | 4.86 | 1421 | 7410 | Subaerical landslides | [108] |
| Hattian Bala | 0.307 | 0.98 | 0.202 | 737 | 2400 | Subaerical landslides | [109] |
| Mont Blanc Massif | 0.258 | 0.018 | / | 1860 | 7200 | Subaerical landslides | [110] |
| MountStelle | 0.24 | 0.06 | / | 2188 | 9120 | Subaerical landslides | [111] |
| Montserrat | 0.25 | 0.04 | / | 875 | 3500 | Subaerical landslides | [3] |
| Soufrière Guadeloupe | 0.142 | 0.5 | 25 | 1350 | 9500 | Volcanic landslides | [112] |
| St. Helens 20,000 BP | 0.109 | 1 | / | 1750 | 16,000 | Volcanic landslides | [112] |
| Vesuvius 1944 | 0.898 | 0.000179 | 0.022 | 575 | 640 | Volcanic landslides | [113] |
| Vesuvius 1944 | 0.537 | 0.0009 | 0.113 | 505 | 940 | Volcanic landslides | [113] |
| Vesuvius 1944 | 0.570 | 0.00055 | 0.099 | 285 | 500 | Volcanic landslides | [113] |
| Vesuvius 1944 | 0.490 | 0.000793 | 0.126 | 470 | 960 | Volcanic landslides | [113] |
| Vesuvius 1944 | 0.513 | 0.001 | 0.136 | 636 | 1240 | Volcanic landslides | [113] |
| Vesuvius 1944 | 0.529 | 0.0011 | 0.145 | 360 | 680 | Volcanic landslides | [113] |
| Vesuvius | 0.500 | 0.00116 | 0.161 | 410 | 820 | Volcanic landslides | [113] |
| Jocotitlan | 0.096 | 2.8 | 80 | 1150 | 12,000 | Volcanic landslides | [112] |
| Akagi | 0.126 | 4 | / | 2400 | 19,000 | Volcanic landslides | [100] |
| Asakusa | 0.154 | 0.04 | / | 1000 | 6500 | Volcanic landslides | [100] |
| Asama | 0.090 | 2 | 90 | 1800 | 20,000 | Volcanic landslides | [100] |
| Bandaisan | 0.109 | 1.5 | 34 | 1200 | 11,000 | Volcanic landslides | [100] |
| Bezymianni | 0.133 | 0.8 | 30 | 2400 | 18,000 | Volcanic landslides | [100] |
| Callaqui | 0.207 | 0.15 | / | 3100 | 15,000 | Volcanic landslides | [100] |
| Chaos Crags | 0.130 | 0.15 | 8 | 650 | 5000 | Volcanic landslides | [100] |
| Chimborazo | 0.103 | 8.1 | / | 3600 | 35,000 | Volcanic landslides | [100] |
| Chokai | 0.088 | 3.5 | / | 2200 | 25,000 | Volcanic landslides | [100] |
| Colima | 0.100 | 12.5 | 900 | 4000 | 40,000 | Volcanic landslides | [100] |
| Egmont | 0.084 | 7.5 | 250 | 2600 | 31,000 | Volcanic landslides | [100] |
| Egmont | 0.093 | 0.35 | 120 | 2500 | 27,000 | Volcanic landslides | [100] |
| Fuji | 0.104 | 1.8 | / | 2500 | 24,000 | Volcanic landslides | [100] |
| Galunggung | 0.076 | 2.9 | 175 | 1900 | 25,000 | Volcanic landslides | [100] |
| Iriga | 0.095 | 1.5 | 65 | 1050 | 11,000 | Volcanic landslides | [100] |
| Iwaki | 0.114 | 1.3 | / | 1600 | 14,000 | Volcanic landslides | [100] |
| Komagatake | 0.087 | 0.25 | / | 1000 | 11,500 | Volcanic landslides | [100] |
| Kurohime | 0.133 | 0.12 | / | 800 | 6000 | Volcanic landslides | [100] |
| Mageik | 0.089 | 0.09 | / | 800 | 9000 | Volcanic landslides | [100] |
| Mawenzi | 0.075 | 7.1 | 1150 | 4500 | 60,000 | Volcanic landslides | [100] |
| Meru | 0.078 | 15 | 1400 | 3900 | 50,000 | Volcanic landslides | [100] |
| Monbacho | 0.108 | 1 | 45 | 1300 | 12,000 | Volcanic landslides | [100] |
| Mt. St. Helens | 0.106 | 2.5 | 60 | 2550 | 24,000 | Volcanic landslides | [100] |
| Myoko (Sekikawa) | 0.105 | 0.8 | / | 2000 | 19,000 | Volcanic landslides | [100] |
| Myoko (Taguchi) | 0.175 | 0.23 | 10 | 1400 | 8000 | Volcanic landslides | [100] |
| Ovalnaya Zimina | 0.141 | 0.4 | / | 2400 | 17,000 | Volcanic landslides | [100] |
| Papandayan | 0.136 | 0.14 | / | 1500 | 11,000 | Volcanic landslides | [100] |
| Peteroa | 0.046 | 16 | / | 3900 | 85,000 | Volcanic landslides | [100] |
| Popa | 0.109 | 0.8 | / | 1200 | 11,000 | Volcanic landslides | [100] |
| Popocatepetl | 0.121 | 28 | / | 4000 | 33,000 | Volcanic landslides | [100] |
| Shasta | 0.071 | 26 | 450 | 3550 | 50,000 | Volcanic landslides | [100] |
| Shiveluch | 0.167 | 1.5 | 98 | 2000 | 12,000 | Volcanic landslides | [100] |
| Sierra Velluda | 0.136 | 0.5 | / | 3400 | 25,000 | Volcanic landslides | [100] |
| Socompa | 0.093 | 17 | 480 | 3250 | 35,000 | Volcanic landslides | [100] |
| Tashiro | 0.080 | 0.55 | / | 700 | 8800 | Volcanic landslides | [100] |
| Tateshina | 0.112 | 0.35 | / | 1400 | 12,500 | Volcanic landslides | [100] |
| Unzen | 0.131 | 0.34 | 12 | 850 | 6500 | Volcanic landslides | [100] |
| Usu | 0.077 | 0.3 | / | 500 | 6500 | Volcanic landslides | [100] |
| Yatsugatake (Nirasaki) | 0.075 | 9 | / | 2400 | 32,000 | Volcanic landslides | [100] |
| Yatsugatake (Otsukigawa) | 0.112 | 0.27 | 1988/ | 1400 | 12,500 | Volcanic landslides | [100] |
| Kitimat Slide | 0.033 | 0.2 | / | 200 | 6000 | Submarine landslides | [60] |
| A1 | 0.005 | 250 | / | 1700 | 370,000 | Submarine landslides | [60] |
| A2 | 0.009 | 22 | / | 1500 | 160,000 | Submarine landslides | [60] |
| A3 | 0.010 | 8.5 | / | 1400 | 140,000 | Submarine landslides | [60] |
| A4A | 0.010 | 27 | / | 1300 | 130,000 | Submarine landslides | [60] |
| A4B | 0.005 | 320 | / | 2000 | 400,000 | Submarine landslides | [60] |
| Kae Lae slideb | 0.083 | 40 | / | 5000 | 60,000 | Submarine landslides | [60] |
| Molokai slideb | 0.040 | 1100 | / | 5200 | 130,000 | Submarine landslides | [60] |
| Oahu slideb | 0.031 | 1800 | / | 5500 | 180,000 | Submarine landslides | [60] |

**Table A1.** *Cont.*

| Landslides | $H_{max}/L_{max}$ | Volume $V$ (km$^3$) | Area $A$ (km$^2$) | $H_{max}$ | $L_{max}$ | Types of Landslides | References |
|---|---|---|---|---|---|---|---|
| Grant Banks | 0.003 | 76 | / | 365 | 110,000 | Submarine landslides | [61] |
| Hawaii | 0.013 | | / | 2000 | 160,000 | Submarine landslides | [61] |
| Kidnappers | 0.005 | 8 | / | 50 | 11,000 | Submarine landslides | [61] |
| Bay of Biscay | 0.012 | | / | 250 | 21,000 | Submarine landslides | [61] |
| Rockall | 0.002 | 300 | / | 330 | 160,000 | Submarine landslides | [61] |
| Bassein | 0.010 | | / | 360 | 37,000 | Submarine landslides | [61] |
| Agulhas | 0.004 | | / | 375 | 106,000 | Submarine landslides | [61] |
| Copper River Delta | 0.006 | | / | 115 | 18,000 | Submarine landslides | [61] |
| Albatross Bank | 0.057 | | / | 300 | 5300 | Submarine landslides | [61] |
| Portlock Bank | 0.031 | | / | 200 | 6500 | Submarine landslides | [61] |
| Kayak Trough | 0.008 | | / | 115 | 15,000 | Submarine landslides | [61] |
| Atlantic Coast | 0.009 | | / | 30 | 3400 | Submarine landslides | [61] |
| Unnamed | 0.017 | | / | 80 | 4800 | Submarine landslides | [61] |
| Unnamed | 0.008 | | / | 18 | 2300 | Submarine landslides | [61] |
| Magdalena | 0.058 | 0.3 | / | 1400 | 24,000 | Submarine landslides | [61] |
| Valdez | 0.131 | 0.075 | / | 168 | 1280 | Submarine landslides | [61] |
| Mississippi River Delta | / | 0.04 | / | 20 | / | Submarine landslides | [61] |
| Suva | / | 0.15 | / | 100 | / | Submarine landslides | [61] |
| Orkdalsfjord | 0.022 | 0.025 | / | 500 | 22,500 | Submarine landslides | [61] |
| Sandnesjoen | 0.150 | 0.005 | / | 180 | 1200 | Submarine landslides | [61] |
| Sokkelvik | 0.048 | 0.0005 | / | 120 | 2500 | Submarine landslides | [61] |
| Helsinki | 0.028 | 0.000006 | / | 11 | 400 | Submarine landslides | [61] |
| Storegga | 0.011 | 800 | / | 1700 | 160,000 | Submarine landslides | [61] |
| Typical Atlantic Ocean | 0.300 | / | / | 1200 | 4000 | Submarine landslides | [61] |
| Cape Fear | 0.023 | / | / | 700 | 30,000 | Submarine landslides | [61] |
| Blake Escarpment | 0.086 | 600 | / | 3600 | 42,000 | Submarine landslides | [61] |
| East Break East | 0.016 | 13 | | 1150 | 70,000 | Submarine landslides | [61] |
| East Break West | 0.010 | 160 | / | 1100 | 110,000 | Submarine landslides | [61] |
| Navarin Canyon | 0.029 | 5 | / | 175 | 6000 | Submarine landslides | [61] |
| Seward | 0.067 | 0.0027 | / | 200 | 3000 | Submarine landslides | [61] |
| Alsek | 0.010 | / | / | 20 | 2000 | Submarine landslides | [61] |
| Sur | 0.010 | 10 | / | 750 | 75,000 | Submarine landslides | [61] |
| Santa Barbara | 0.052 | 0.02 | / | 120 | 2300 | Submarine landslides | [61] |
| Alika-2b | 0.051 | 300 | / | 4800 | 95,000 | Submarine landslides | [61] |
| Nuuanub | 0.022 | 5000 | / | 5000 | 230,000 | Submarine landslides | [61] |
| Tristan de Cunhab | 0.075 | 150 | / | 3750 | 50,000 | Submarine landslides | [61] |
| Unnamed | 0.059 | 17,880 | 4716 | 7000 | 119,000 | Martian landslides | [56] |
| Unnamed | 0.043 | / | / | 2400 | 56,000 | Martian landslides | [56] |
| Unnamed | 0.100 | 4880 | 1175 | 7000 | 70,000 | Martian landslides | [56] |
| Unnamed | 0.102 | 4183 | 1244 | 8400 | 82,000 | Martian landslides | [56] |
| Unnamed | 0.072 | 4047 | 2200 | 6800 | 94,000 | Martian landslides | [56] |
| Unnamed | 0.085 | / | / | 4400 | 52,000 | Martian landslides | [56] |
| Unnamed | 0.095 | 3267 | 1287 | 7200 | 76,000 | Martian landslides | [56] |
| Unnamed | 0.125 | 2960 | 1675 | 8000 | 64,000 | Martian landslides | [56] |
| Unnamed | 0.108 | 2761 | 1144 | 6800 | 63,000 | Martian landslides | [56] |
| Unnamed | 0.108 | / | / | 5400 | 50,000 | Martian landslides | [56] |
| Unnamed | 0.130 | 1282 | 1244 | 8200 | 63,000 | Martian landslides | [56] |
| Unnamed | 0.096 | 833 | 1075 | 5400 | 56,000 | Martian landslides | [56] |
| Unnamed | 0.080 | 688 | 888 | 3600 | 45,000 | Martian landslides | [56] |
| Unnamed | 0.142 | 668 | 656 | 4400 | 31,000 | Martian landslides | [56] |
| Unnamed | 0.141 | 655 | 470 | 7600 | 54,000 | Martian landslides | [56] |
| Unnamed | 0.150 | 321 | 312 | 5400 | 36,000 | Martian landslides | [56] |
| Unnamed | 0.085 | 157 | 325 | 2800 | 33,000 | Martian landslides | [56] |
| Unnamed | 0.124 | 32 | 125 | 3600 | 29,000 | Martian landslides | [56] |
| Unnamed | 0.200 | 29 | 350 | 4000 | 20,000 | Martian landslides | [56] |
| Unnamed | 0.111 | 98 | 175 | 2000 | 18,000 | Martian landslides | [56] |
| Unnamed | 0.150 | 11 | 44 | 1200 | 8000 | Martian landslides | [56] |
| Unnamed | 0.305 | 38.5 | 84 | 6400 | 21,000 | Martian landslides | [56] |
| Unnamed | 0.310 | 37.1 | 81 | 6200 | 20,000 | Martian landslides | [56] |
| Unnamed | 0.326 | 30.1 | 66 | 6200 | 19,000 | Martian landslides | [56] |
| Unnamed | 0.313 | 23.1 | 50 | 5000 | 16,000 | Martian landslides | [56] |
| Unnamed | 0.365 | 9.8 | 22 | 6200 | 17,000 | Martian landslides | [56] |
| Unnamed | 0.314 | 6.3 | 13 | 2200 | 7000 | Martian landslides | [56] |
| Unnamed | 0.367 | 2.1 | 4 | 2200 | 6000 | Martian landslides | [56] |
| Ophir | 0.14 | 833 | / | 7280 | 52,000 | Martian landslides | [114] |
| OphirWest | 0.15 | 1500 | / | 7050 | 47,000 | Martian landslides | [114] |
| Coprates | 0.08 | 730 | / | 4960 | 62,000 | Martian landslides | [114] |
| Ius | 0.12 | 2600 | / | 7920 | 66,000 | Martian landslides | [114] |
| GangesLandslide1 | 0.10 | 530 | / | 5000 | 50,000 | Martian landslides | [114] |
| GangesLandslide2 | 0.13 | 19 | / | 2899 | 22,300 | Martian landslides | [3] |
| GangesLandslide3 | 0.14 | 9.95 | / | 3124 | 22,316 | Martian landslides | [3] |

**Table A1.** *Cont.*

| Landslides | $H_{max}/L_{max}$ | Volume $V$ (km$^3$) | Area $A$ (km$^2$) | $H_{max}$ | $L_{max}$ | Types of Landslides | References |
|---|---|---|---|---|---|---|---|
| Olympus Mons | 0.40 | 0.165 | / | 1384 | 3460 | Martian landslides | [3] |
| Crater ManySlides1 | 0.24 | 0.0311 | / | 434 | 1810 | Martian landslides | [3] |
| Crater ManySlides2 | 0.23 | 0.0576 | / | 499 | 2169 | Martian landslides | [3] |
| Crater ManySlides3 | 0.30 | 0.0349 | / | 576 | 1920 | Martian landslides | [3] |
| Equatorial Crater | 0.13 | 11.3 | / | 598 | 4600 | Martian landslides | [3] |
| ShalbatanaVallis1 | 0.07 | 31.9 | / | 805 | 11,500 | Martian landslides | [3] |
| ShalbatanaVallis2 | 0.20 | 1 | / | 1120 | 5600 | Martian landslides | [3] |
| Malun | 0.123 | 24,000 | / | 7995 | 65,000 | Iapetus landslides | [3] |
| Iapetus2 | 0.118 | 1600 | / | 9440 | 80,000 | Iapetus landslides | [111] |
| Iapetus3 | 0.133 | 3000 | / | 7980 | 60,000 | Iapetus landslides | [111] |
| EuboeaMontes | 0.084 | 25,000 | / | 6804 | 81,000 | Io landslides | [3] |
| Yigong Landslide | 0.416 | 2.8~3 | 5 | 7280 | 8000 | Subaerical landslides | [19] |
| Landslide in Xikou Town | 0.483 | 0.0172 | / | 724 | 1500 | Subaerical landslides | [17] |
| Touzhaigou Landslide | 0.271 | 0.2 | / | 760 | 2800 | Subaerical landslides | [115] |
| Jiwei Mountain Landslide | 0.273 | 0.05 | 0.84 | 600 | 2200 | Subaerical landslides | [70] |
| Guanling Dazhai Landslide | 0.280 | 0.0179 | 0.72 | 420 | 1500 | Subaerical landslides | [72] |
| Donghekou | 0.267 | 0.15 | 1.28 | 640 | 2400 | Subaerical landslides | [48] |
| Zhaojiagou Landslide | 0.347 | 0.002 | / | 260 | 750 | Subaerical landslides | [116] |
| Shale Mountain Landslide | 0.187 | 0.05 | / | 300 | 1600 | Subaerical landslides | [116] |
| Sanxi Landslide | 0.299 | 0.015 | / | 377 | 1260 | Subaerical landslides | [117] |
| Pufu Landslide 1 | 0.340 | 0.45 | 1.1 | 1700 | 5000 | Subaerical landslides | [16] |
| Pufu Landslide 2 | 0.344 | 0.00005 | / | 1100 | 3200 | Subaerical landslides | [16] |
| Wenjiagou | 0.330 | 0.5 | 3 | 1320 | 4000 | Subaerical landslides | [50] |
| Shuimogou | 0.430 | 0.2 | 0.91 | 860 | 2000 | Subaerical landslides | [50] |
| Large House Foundation | 0.463 | 0.163 | 0.79 | 880 | 1900 | Subaerical landslides | [50] |
| Hongshigou | 0.385 | 0.134 | 0.68 | 1040 | 2700 | Subaerical landslides | [50] |
| Before The Nest | 0.350 | 0.12 | 0.59 | 560 | 1600 | Subaerical landslides | [50] |
| Xiaojia Mountain | 0.689 | 0.078 | 0.46 | 930 | 1350 | Subaerical landslides | [50] |
| Niumian Gou | 0.303 | 0.075 | 0.52 | 800 | 2640 | Subaerical landslides | [50] |
| Establish A Ditch | 0.433 | 0.0536 | 0.35 | 650 | 1500 | Subaerical landslides | [50] |
| Caocaoping | 0.433 | 0.0533 | 0.35 | 580 | 1340 | Subaerical landslides | [50] |
| Huoshi Gou | 0.530 | 0.0468 | 0.32 | 700 | 1320 | Subaerical landslides | [50] |
| Shibangou Village | 0.361 | 0.045 | 0.49 | 650 | 1800 | Subaerical landslides | [50] |
| Xiejiadianzi | 0.450 | 0.04 | 0.29 | 720 | 1600 | Subaerical landslides | [50] |
| Dashigou | 0.400 | 0.0314 | 0.24 | 560 | 1400 | Subaerical landslides | [50] |
| Changping | 0.417 | 0.0283 | 0.22 | 500 | 1200 | Subaerical landslides | [50] |
| Xiaomuling | 0.693 | 0.0273 | 0.21 | 710 | 1025 | Subaerical landslides | [50] |
| Baishuling | 0.517 | 0.0256 | 0.20 | 620 | 1200 | Subaerical landslides | [50] |
| Dawan Bay | 0.480 | 0.0248 | 0.20 | 480 | 1000 | Subaerical landslides | [50] |
| Zengjia Mountain | 0.573 | 0.0239 | 0.19 | 650 | 1135 | Subaerical landslides | [50] |
| Shi Zhouzi | 0.533 | 0.0192 | 0.16 | 640 | 1200 | Subaerical landslides | [50] |
| Long Beach | 0.636 | 0.0163 | 0.15 | 1050 | 1650 | Subaerical landslides | [50] |
| Hongma Gong | 0.413 | 0.0154 | 0.14 | 330 | 800 | Subaerical landslides | [50] |
| Baiguo Village | 0.325 | 0.0147 | 0.14 | 260 | 800 | Subaerical landslides | [50] |
| Qinglong Village | 0.333 | 0.0138 | 0.13 | 200 | 600 | Subaerical landslides | [50] |
| Pengjiashan | 0.580 | 0.0129 | 0.12 | 580 | 1000 | Subaerical landslides | [50] |
| Longwan Village | 0.535 | 0.0092 | 0.10 | 460 | 860 | Subaerical landslides | [50] |
| Zhang Zhengbo | 0.400 | 0.0091 | 0.10 | 320 | 800 | Subaerical landslides | [50] |
| Du Jiayan | 0.455 | 0.0086 | 0.094 | 400 | 880 | Subaerical landslides | [50] |
| Ma Flooring | 0.534 | 0.0085 | 0.094 | 395 | 740 | Subaerical landslides | [50] |
| Rock Watchtower Nest | 0.488 | 0.0082 | 0.092 | 390 | 800 | Subaerical landslides | [50] |
| Window Ditch | 0.440 | 0.0081 | 0.091 | 295 | 670 | Subaerical landslides | [50] |
| Zhao Jiashan | 0.400 | 0.007 | 0.082 | 280 | 700 | Subaerical landslides | [50] |
| Weiziping | 0.400 | 0.006 | 0.074 | 240 | 600 | Subaerical landslides | [50] |
| Caterpillar Mountain 2 # | 0.676 | 0.0056 | 0.070 | 500 | 740 | Subaerical landslides | [50] |
| Waqian Mountain | 0.403 | 0.0056 | 0.070 | 250 | 620 | Subaerical landslides | [50] |
| Muhongping | 0.433 | 0.0054 | 0.068 | 420 | 970 | Subaerical landslides | [50] |
| Daping Shang | 0.570 | 0.0051 | 0.065 | 365 | 640 | Subaerical landslides | [50] |
| Liushuping 2 | 0.414 | 0.004 | 0.054 | 240 | 580 | Subaerical landslides | [50] |
| Luanshibao Landslide | 0.200 | 0.7 | 4.36 | 821 | 4100 | Subaerical landslides | [50] |
| Big Light Bag | 0.429 | 7.42 | 6.2 | 1500 | 3500 | Subaerical landslides | [49] |
| Sucun Landslide | 0.239 | 0.004 | 0.235 | 320 | 1340 | Subaerical landslides | [52] |
| Hongao Landslide | 0.180 | 0.0232 | 0.385 | 126 | 700 | Subaerical landslides | [118] |
| Xinmo Landslide | 0.448 | 0.045 | / | 1120 | 2500 | Subaerical landslides | [73] |
| Walai Landslide | 0.320 | 0.51 | / | 1115 | 3480 | Subaerical landslides | [119] |
| Shuicheng Landslide | 0.366 | 0.0191 | 0.3 | 474 | 1296 | Subaerical landslides | [53] |
| Nixu Landslide | 0.184 | 0.33 | 0.55 | 860 | 4670 | Subaerical landslides | [120] |
| Heifangtai Landslide | 0.184 | 0.0127 | 0.1015 | 160 | 870 | Subaerical landslides | [67] |
| Yushu Bingda Landslide | 0.308 | 0.00009 | / | 552 | 1795 | Subaerical landslides | [69] |

**Table A2.** Equations of the best power-law fits of data of the long-runout landslides in Figure 2.

| | Best Power-Law Fit | $R^2$ |
|---|---|---|
| Graph of $L_{max}$ versus V (Figure 2a) | | |
| Subaerial non-volcanic landslides | $L_{max} = 8V^{0.28}$ | 0.40 |
| Subaerial volcanic landslides | $L_{max} = 17V^{0.38}$ | 0.67 |
| Submarine landslides | $L_{max} = 52V^{0.18}$ | 0.42 |
| Martian landslides | $L_{max} = 7V^{0.3}$ | 0.94 |
| Graph of $H_{max}/L_{max}$ versus V (Figure 2b) | | |
| Subaerial non-volcanic landslides | $H_{max}/L_{max} = 0.27V^{-0.07}$ | 0.20 |
| Subaerial volcanic landslides | $H_{max}/L_{max} = 0.12V^{-0.25}$ | 0.93 |
| Submarine landslides | $H_{max}/L_{max} = 0.04V^{-0.05}$ | 0.11 |
| Martian landslides | $H_{max}/L_{max} = 0.44V^{-0.20}$ | 0.68 |
| Graph of $H_{max}/L_{max}$ versus $L_{max}$ (Figure 2c) | | |
| Subaerial non-volcanic landslides | $H_{max}/L_{max} = 0.43L_{max}{}^{-0.20}$ | 0.42 |
| Subaerial volcanic landslides | $H_{max}/L_{max} = 0.60L_{max}{}^{-0.65}$ | 0.89 |
| Submarine landslides | $H_{max}/L_{max} = 0.07L_{max}{}^{-0.24}$ | 0.11 |
| Martian landslides | $H_{max}/L_{max} = 0.85L_{max}{}^{-0.48}$ | 0.57 |

## References


1. Legros, F. The mobility of long-runout landslides. *Eng. Geol.* **2002**, *63*, 301–331. [CrossRef]
2. Locat, P.; Couture, R.; Leroueil, S.; Locat, J.; Jaboyedoff, M. Fragmentation energy in rock avalanches. *Can. Geotech. J.* **2006**, *43*, 830–851. [CrossRef]
3. Lucas, A.; Mangeney, A.; Ampuero, J. Frictional velocity-weakening in landslides on Earth and on other planetary bodies. *Nat. Commun.* **2014**, *5*, 3417. [CrossRef]
4. Yin, Y.; Liu, C.; Chen, H.; Ren, J.; Zhu, C. Investigation on catastrophic landslide of January 11, 2013 at ZhaoJiaGou, ZhenXiong County, YunNan Province. *J. Eng. Geol.* **2013**, *21*, 6–15.
5. Hungr, O. Rock avalanche occurrence, process and modelling. *Landslides Massive Rock Slope Fail.* **2006**, *49*, 243–266. [CrossRef]
6. Cheng, Q.; Zhang, Z.; Huang, R. Study on dynamics of rock avalanches: State of the art report. *J. Mt. Sci.* **2007**, *25*, 72–84.
7. Zhang, M.; Yin, Y.; Wu, S.; Zhang, Y. Development status and prospects of studies on kinematics of long-runout rock avalanches. *J. Eng. Geol.* **2010**, *18*, 805–817.
8. Korup, O.; Schneider, D.; Huggel, C.; Dufresne, A. 7.18 Long-Runout Landslides. *Treatise Geomorphol.* **2013**, *7*, 183–199. [CrossRef]
9. Li, K.; Wang, Y.; Lin, Q.; Chen, Q.; Wu, Y. Experiments on granular flow behavior and deposit characteristics: Implications for rock avalanche kinematics. *Landslides* **2021**, *18*, 1779–1799. [CrossRef]
10. Gary, M.; McAffe, R.; Wolf, C. *Glossary of Geology*; American Geological Institute: Washington, DC, USA, 1972; p. 805.
11. International Union of Geological Sciences Working Group on Landslide. A suggested method for describing the rate of movement of a landslide. *Bull. Int. Assoc. Eng. Geol.* **1995**, *52*, 75–78. [CrossRef]
12. Heim, A. *Bergsturz und Menschenleben*; Fretz and Wasmuth Verlag: Zurich, Switzerland, 1932; p. 218.
13. Buss, E.; Heim, A. Der Bergsturz von Elm. *Z. Der Dtsch. Geol. Ges.* **1881**, *33*, 540–564.
14. Plafker, G.; Ericksen, G. Ericksen Nevados Huascaran avalanches Peru. *Dev. Geotech. Eng.* **1978**, *14*, 277–314. [CrossRef]
15. Dunning, S.; Mitchell, W.; Rosser, N.; Petley, D. The Hattian Bala rock avalanche and associated landslides triggered by the Kashmir Earthquake of 8 October 2005. *Eng. Geol.* **2007**, *93*, 130–144. [CrossRef]
16. Cheng, X.; Zhu, C.; Qi, W.; Qi, J.; Yuan, J. Formation conditions, development tendency and preventive measures of Pufu landslide in Luquan of Yunnan. *Miner. Resour. Geol.* **2015**, *29*, 395–401.
17. Zhong, L. Geological disaster development mechanism and their prevention countermeasures in the "Three Rivers" juxtaposition area, Yunnan Province. *Chin. J. Geol. Hazard Control* **2007**, *4*, 6.
18. Hu, M.; Cheng, Q.; Wang, F. Experimental study on formation of YiGong long-distance high-speed landslide. *J. Rock Mech. Eng.* **2009**, *28*, 138–143.
19. Yin, Y. Study of the giant landslide of Bomi Yigong expressway in Tibet. *Chin. J. Geol. Hazard Control* **2000**, *11*, 103. [CrossRef]
20. Wang, T.; Shi, J.; Wu, S.; Zhang, Y.; Li, B. Formation mechanism of wenjiagou high-speed and long-runout debris avalanche triggered by WenChuan earthquake. *J. Eng. Geol.* **2008**, *18*, 631–644.
21. Pudasaini, P.; Miller, S. The hypermobility of huge landslides and avalanches. *Eng. Geol.* **2013**, *157*, 124–132. [CrossRef]
22. Hewitt, K. Catastrophic landslide deposits in the karakoram Himalaya. *Science* **1988**, *242*, 64–67. [CrossRef]

23. Davies, T.; McSaveney, M.; Hodgson, K. A fragmentation-spreading model for long-runout rock avalanches. *Can. Geotech. J.* **1999**, *36*, 1096–1110. [CrossRef]
24. Bowman, E.; Take, W.; Rait, K.; Hann, C. Physical models of rock avalanche spreading behaviour with dynamic fragmentation. *Can. Geotech. J.* **2012**, *49*, 460–476. [CrossRef]
25. Hardin, O. Crushing of Soil Particles. *J. Geotech. Eng.* **1985**, *111*, 1177. [CrossRef]
26. Lin, Q.; Chen, Q.; Li, K.; Wang, Y.; Liu, S. Review on fragmentation-related dynamics of rock avalanches. *J. Eng. Geol.* **2023**, *31*, 815–829. [CrossRef]
27. Strom, A. Morphology and internal structure of rockslides and rock avalanches: Grounds and constraints for their modelling. In *Landslides from Massive Rock Slope Failure*; Springer: Dordrecht, The Netherlands, 2006; pp. 305–326. [CrossRef]
28. Friedmann, S.; Taberlet, N.; Losert, W. Rock-avalanche dynamics: Insights from granular physics experiments. *Int. J. Earth Sci.* **2006**, *95*, 911–919. [CrossRef]
29. Crosta, G.; Frattini, P.; Fusi, N. Fragmentation in the Val Pola rock avalanche, Italian Alps. *J. Geophys. Res.* **2007**, *112*, F01006. [CrossRef]
30. Gray, J. Particle segregation in dense granular flow. *Annu. Rev. Fluid Mech.* **2018**, *50*, 407–433. [CrossRef]
31. Yu, F.; Su, L. Experimental investigation of mobility and deposition characteristics of dry granular flow. *Landslides* **2021**, *18*, 1875–1887. [CrossRef]
32. Hu, W.; Chang, C.; McSaveney, M.; Huang, R.; Xu, Q.; Zheng, Y.; Yu, J. A weakening rheology of dry granular flows with extensive brittle grain damage in high-speed rotary shear experiments. *Geophys. Res. Lett.* **2020**, *47*, e2020GL087763. [CrossRef]
33. Wang, Z.; Wang, G. Effect of particle breakage-induced frictional weakening on the dynamics of landslides. *Granul. Matter* **2022**, *24*, 72. [CrossRef]
34. Schneider, J.; Fisher, R.V. Transport and emplacement mechanisms of large volcanic debris avalanches: Evidence from the northwest sector of Cantal Volcano (France). *J. Volcanol. Geotherm. Res.* **1998**, *83*, 141–165. [CrossRef]
35. Cruden, D.; Hungr, O. The debris of the Frank Slide and theories of rockslide-avalanche mobility. *Can. J. Earth Sci.* **1986**, *23*, 425–432. [CrossRef]
36. Xiao, Y.; Liu, H.; Yang, G.; Chen, Y.; Jiang, J. A constitutive model for the state-dependent behaviors of rockfill material considering particle breakage. *Sci. China Technol. Sci.* **2014**, *57*, 1636–1646. [CrossRef]
37. Yu, F. Particle breakage in granular soils: A review. *Part. Sci. Technol.* **2019**, *39*, 91–100. [CrossRef]
38. Yu, F.; Su, L.; Peng, X. Influence of particle breakage on the isotropic compressibility of sands. *J. Mt. Sci.* **2022**, *19*, 2086–2099. [CrossRef]
39. Wang, F.; Sassa, K.; Wang, G. Mechanism of a long-runout landslide triggered by the August 1998 heavy rainfall in Fukushima Prefecture, Japan. *Eng. Geol.* **2002**, *63*, 169–185. [CrossRef]
40. Ottino, J.; Khakhar, D. Mixing and segregation of granular materials. *Annu. Rev. Fluid Mech.* **2000**, *32*, 55–91. [CrossRef]
41. Zhou, D.; Hg, C. Numerical investigation of reverse segregation in debris flows by DEM. *Granul. Matter* **2010**, *12*, 507–516. [CrossRef]
42. Kokelaar, B.; Graham, R.; Gray, J.; Vallance, J.W. Fine-grained linings of leveed channels facilitate runout of granular flows. *Earth Planet. Sci. Lett.* **2014**, *385*, 172–180. [CrossRef]
43. Zhou, G.; Sun, Q.; Cui, P. Study on the mechanisms of solids segregation in granular debris flows. *J. SiChuan Univ. Eng. Sci. Ed.* **2013**, *45*, 28–36. [CrossRef]
44. Li, T.; Fan, X.; Jiang, Y. A study on inverse grading and its influence on impact effect of landslide-debris flow. *Yangtze River* **2018**, *49*, 58–65. [CrossRef]
45. Kent, P. The transport mechanism in catastrophic rock Falls. *J. Geol.* **1966**, *74*, 79–83. [CrossRef]
46. Shreve, R. Sherman Landslide, Alaska. *Science* **1966**, *154*, 1639–1643. [CrossRef]
47. Wu, S.; Wang, T.; Shi, L.; Sun, P.; Shi, J. Study on catastrophic landslides triggered by 2008 great WenChuan earthquake, Sichuan, China. *J. Eng. Geol.* **2010**, *18*, 145–159.
48. Qi, C.; Xing, A.; Yin, Y.; Li, B. Numerical simulation of dynamic behavior of donghekou rockslide-debris avalanche. *J. Eng. Geol.* **2012**, *20*, 334–339.
49. Zhang, W.; Huang, R.; Pei, X. Analysis on kinematics characteristics and movement process of Daguangbao landslide. *J. Eng. Geol.* **2015**, *23*, 866–885. [CrossRef]
50. Zhan, W.; Huang, R.; Pei, X.; Li, W. Empirical prediction model for movement distance of gully type rock avalanches. *J. Eng. Geol.* **2017**, *25*, 154–163. [CrossRef]
51. Sassa, K. Geotechnical model for the motion of landslides. In Proceedings of the 5th International Symposium on Landslides, Lausanne, Switzerland, 10–15 July 1988; pp. 37–55.
52. Gan, J.; Fan, J.; Tang, C.; Wang, C.; Liu, Z. Sucun landslide in suichang county of zejiang province: Characteristicesand failure mechanism. *J. Catastrophology* **2017**, *32*, 73–78. [CrossRef]

53. Zheng, G.; Xu, Q.; Liu, X.; Li, Y.; Dong, X.; Ju, N.; Guo, C. The JiChang landslide on July 23, 2019 in ShuiCheng, GuiZhou: Characteristics and failure mechanism. *J. Eng. Geol.* **2020**, *28*, 541–556. [CrossRef]
54. Yu, F.; Su, L.; Li, X.; Zhao, Y. Impact dynamics of granular flow on rigid barriers: Insights from numerical investigation using material point method. *J. Mt. Sci.* **2024**, *21*, 4083–4111. [CrossRef]
55. Yu, F.; Su, L.; Li, X.; Zhao, Y. Mobility and dynamic erosion process of granular flow: Insights from numerical investigation using material point method. *J. Mt. Sci.* **2024**, *21*, 2713–2738. [CrossRef]
56. McEwen, A. Mobility of large rock avalanches: Evidence from Valles Marineris, Mars. *Geology* **1989**, *17*, 1111–1114. [CrossRef]
57. Crosta, G.; Frattini, P.; Valbuzzi, E.; Blasio, F. Introducing a new inventory of large martian landslides. *Earth Space Sci.* **2018**, *5*, 89–119. [CrossRef]
58. Watkins, J.A.; Ehlmann, B.L.; Yin, A. Long-runout landslides and the long-lasting effects of early water activity on Mars. *Geol. Soc. Am.* **2015**, *43*, 107–110. [CrossRef]
59. Johnson, B.; Campbell, C. Drop height and volume control the mobility of long-runout landslides on the Earth and Mars. *Geophys. Res. Lett.* **2017**, *44*, 12091–12097. [CrossRef]
60. Lipman, P.; Normark, W.; Moore, J.; Wilson, J.; Gutmacher, C. The giant submarine Alika debris slide, Mauna Loa, Hawaii. *J. Geophys. Res. Soild Earth* **1988**, *93*, 4279–4299. [CrossRef]
61. Hampton, M.; Lee, H.; Locat, J. Submarine landslides. *Rev. Geophys.* **1996**, *34*, 33–59. [CrossRef]
62. Masson, D.; Harbitz, C.; Wynn, R.; Pedersen, G.; Løvholt, F. Submarine landslides: Processes, triggers and hazard prediction. *Philos. Trans. R. Soc. A* **2006**, *304*, 2009–2039. [CrossRef]
63. Harbitz, C.; Løvholt, F.; Bungum, H. Submarine landslide tsunamis:how extreme and how likely? *Nat. Hazards* **2014**, *72*, 1341–1374. [CrossRef]
64. Iverson, R. The physics of debris flows. *Rev. Geophys.* **1997**, *35*, 245–296. [CrossRef]
65. Moore, J.; Normark, W.; Holcomb, R. Giant Hawaiian landslides. *Earth Sci.* **1994**, *22*, 119–144. [CrossRef]
66. Liu, P.; Lv, Q.; Wu, J.; Ma, J.; Liao, Z. A flume model test to investigate initation mechanisms of rainsstorm-induced shallow landslides. *J. Eng. Geol.* **2024**, *33*, 531–540. [CrossRef]
67. Pan, R.; Liang, L.; Zhu, Y.; Wang, G. Field investigation and motion simulation study of high-speed long-range landslide in yushu, qinghai-tibet. *Ind. Constr.* **2023**, *53*, 579–584.
68. Huang, R. Mechanism and geomechanical modes of landslide hazards triggered by WenChuan 8.0 earthquake. *Chin. J. Rock Mech. Eng.* **2009**, *28*, 1239–1249.
69. Guo, F.; Zhang, L.; Wang, X.; Song, X. Analysis on evolution process and movement mechanism of the Luojiapo landslide in Heifangtai, Gansu Province. *Chin. J. Geol. Hazard Control* **2023**, *34*, 11–20. [CrossRef]
70. Xu, Q.; Huang, R.; Yin, Y.; Hou, S.; Dong, X.; Fan, X.; Tang, M. The Jiweishan landslide of June 5, 2009 in WuLong, ChongQing:characteristics and failure mechanis. *J. Eng. Geol.* **2009**, *17*, 433–444.
71. Feng, Z.; You, Y.; Chen, L.; Wang, L. Numerical simulation study on kinematic post-failure process of large-scale landslide in the bailong river basin. *J. Catastrophology* **2024**, *39*, 45–50. [CrossRef]
72. Yin, Y.; Zhu, J.; Yang, Y. Investigation of a high speed and long run-out rockslide-debris flow at DaZhai in GuanLing of GuiZhou province. *J. Eng. Geol.* **2010**, *18*, 445–454.
73. Xu, Q.; Li, W.; Dong, X.; Xiao, X.; Fan, X.; Pei, X. The Xinmocun landslide on June 24,2017 in Maoxian, Sichuan: Characteristics and failure mechanism. *Chin. J. Rock Mech. Eng.* **2017**, *36*, 2612–2628. [CrossRef]
74. Hsu, K.J. Catastrophic Debris Streams (Sturzstroms) Generated by Rockfalls. *GSA Bull.* **1975**, *86*, 129–140. [CrossRef]
75. He, K.; Wang, Y.; Chen, Q.; Li, Q.; Shi, A. Research on the substrate entrainment dynamics of rock avalanches: State of the art. *J. Eng. Geol.* **2024**, *32*, 904–917. [CrossRef]
76. Davies, T. Spreading of rock avalanche debris by mechanical fluidization. *Rock Mech.* **1982**, *15*, 9–24. [CrossRef]
77. Li, K.; Cheng, Q.; Lin, Q.; Wang, Y.; Song, Z. State of the art on rock avalanche dynamics from granular flow mechanics. *Earth Sci.* **2022**, *47*, 893–912. [CrossRef]
78. Liu, Z.; Ma, C.; Miao, T.; Mu, Q. Kinematic block model of long run-out prediction for high-speed landslides. *Chin. J. Rock Mech. Eng.* **2000**, *19*, 742–746.
79. Okura, Y.; Kitahara, H.; Sammori, T.; Kawanami, A. The effects of rockfall volume on runout distance. *Eng. Geol.* **2000**, *58*, 109–124. [CrossRef]
80. Melosh, H. Acoustic fluidization: A new geologic process. *J. Geophys. Res. Soild Earth* **1979**, *84*, 7513–7520. [CrossRef]
81. Collins, G.; Melosh, H. Acoustic fluidization and the extraordinary mobility of sturzstroms. *J. Geophys. Res. Soild Earth* **2003**, *108*, B102473. [CrossRef]
82. Heaton, T.H. Evidence for and implications of self-healing pulses of slip in earthquake rupture. *Phys. Earth Planet. Inter.* **1990**, *64*, 1–20. [CrossRef]
83. Tsutsumi, A.; Shimamoto, T. High velocity frictional properties of gabbro. *Geophys. Res. Lett.* **1997**, *24*, 699–702. [CrossRef]
84. Rice, R. Heating and weakening of faults during earthquake slip. *J. Geophys. Res. Soild Earth* **2006**, *111*, B05311. [CrossRef]

85. Goren, L.; Aharonov, E. Long runout landslides: The role of frictional heating and hydraulic diffusivity. *Geophys. Res. Lett.* **2007**, *34*, L07301. [CrossRef]
86. Beeler, N.; Tullis, T.; Goldsby, D. Constitutive relationships and physical basis of fault strength due to flash heating. *J. Geophys. Res. Soild Earth* **2008**, *113*, B01401. [CrossRef]
87. Goldsby, D.L.; Tullis, T.E. Flash heating leads to low frictional strength of crustal rocks at earthquake slip rates. *Science* **2011**, *334*, 216–218. [CrossRef]
88. Zhang, H.; Liu, W.; He, S.; Hu, W. A thermo-poro-mechanics model predicts the transition from creep to rapid movement of large landslides. *Rock Mech. Rock Eng.* **2024**, *57*, 8243–8261. [CrossRef]
89. GDR MiDi. On dense granular flows. *Eur. Phys. J. E* **2004**, *14*, 341–365. [CrossRef]
90. da Cruz, F.; Emam, S.; Prochnow, M.; Roux, J.; Chevoir, F. Rheophysics of dense granular materials: Discrete simulation of plane shear flows. *Phys. Rev. E* **2005**, *72*, 021309. [CrossRef]
91. Jop, P.; Forterre, Y.; Pouliquen, O.A. Constitutive law for dense granular flows. *Nature* **2006**, *441*, 727–730. [CrossRef]
92. Hatano, T. Power-law friction in closely packed granular materials. *Phys. Rev. E* **2007**, *75*, 060301. [CrossRef]
93. Ding, Z.; Hu, W.; Chang, C.; Li, Y.; Wang, G. Shear behaviors of confined flow: Insights for understanding the influences of fractal particle size distribution on high mobility of granular flows. *Geophys. Res. Lett.* **2024**, *51*, e2024GL108956. [CrossRef]
94. Hu, W.; Zheng, Y.; McSaveney, M.; Xu, Q.; Asch, T. Fluidization of bed material caused by shear thinning during rock avalanche entrainment: Insights from flume tests and rheological experiments. *Eng. Geol.* **2023**, *325*, 107276. [CrossRef]
95. Wang, Y.; Lin, Q.; Li, K.; Shi, A.; Li, T. Review on rock avalanche dynamics. *J. Earth Sci. Environ.* **2021**, *43*, 164–181. [CrossRef]
96. Harrison, J.; Falcon, N. An ancient landslip at saidmarreh in southwestern iran. *J. Geol.* **1938**, *46*, 296–309. Available online: http://www.jstor.org/stable/30081302 (accessed on 1 October 2025). [CrossRef]
97. Bock, C. Martinez Mountain rock avalanche. *Rev. Eng. Geol.* **1977**, *3*, 155–168. [CrossRef]
98. Moore, D.; Mathews, W. The Rubble Creek landslide, southwestern British Columbia. *Can. J. Earth Sci.* **1978**, *15*, 1039–1052. [CrossRef]
99. Evans, S.; Clague, J.J.; Woodsworth, G.J.; Hungr, O. The Pandemonium Creek rock avalanche, British Columbia. *Can. Geotech. J.* **1989**, *26*, 427–446. [CrossRef]
100. Hayashi, J.; Self, S. A comparison of pyroclastic flow and debris avalanche mobility. *J. Geophys. Res. Soild Earth* **1992**, *97*, 9063–9071. [CrossRef]
101. Azzoni, A.; Chiesa, S.; Frassoni, A.; Govi, M. The Valpola landslide. *Eng. Geol. J.* **1992**, *33*, 123–139. [CrossRef]
102. Anma, S.; Maikuma, H.; Yoshimura, M.; Fujita, Y.; Okusa, S. Dynamics of earthquake-induced slope failure of Ontake. *Int. J. Rock Mech. Min. Sci. Geomech.* **1989**, *26*, 89. [CrossRef]
103. Voight, B.; Janda, R.; Glicken, H.; Douglass, P. Nature and mechanics of the Mount St.Helens rockslide-avalanche of 18 May 1980. *Geotechnique* **1980**, *33*, 243–273. [CrossRef]
104. Voight, B.; Sousa, J. Lessons from Ontake-san: A comparative analysis of debris avalanche dynamics. *Eng. Geol.* **1994**, *38*, 261–297. [CrossRef]
105. Clague, J.; Souther, J. The Dusty Creek landslide on Mount Cayley, British Columbia. *Can. J. Earth Sci.* **1982**, *19*, 524–539. [CrossRef]
106. Lu, Z.; Cruden, D. Two debris flow modes on Mount Cayley, British Columbia. *Can. Geotech. J.* **1996**, *33*, 123–139. [CrossRef]
107. Schuster, R.L.; Alford, D. Usoi landslide dam and lake sarez, pamir mountains, tajikistan. *Environ. Eng. Geosci.* **2004**, *10*, 151–168. [CrossRef]
108. Evans, G.; Roberts, J.; Ischuk, A.; Delaney, K.; Morozova, G.; Tutubalina, O. Landslides triggered by the 1949 Khait earthquake, Tajikistan, and associated loss of life. *Eng. Geol.* **2009**, *109*, 195–212. [CrossRef]
109. Basharat, M.; Rohn, J.; Ehret, D.; Baig, M. Lithological and structural control of Hattian Bala rock avalanche triggered by the Kashmir earthquake 2005, sub-Himalayas, northern Pakistan. *J. Earth Sci.* **2012**, *23*, 213–224. [CrossRef]
110. Akçar, N.; Deline, P.; Ivy-Ochs, S.; Alfimov, V.; Hajdas, I.; Kubik, K.W.; Christl, M.; Schlüchter, C. The AD 1717 rock avalanche deposits in the upper Ferret Valley (Italy): A dating approach with cosmogenic $^{10}$Be. *J. Quat. Sci.* **2012**, *27*, 383–392. [CrossRef]
111. Singer, K.N.; McKinnon, W.; Schenk, P.; Moore, J. Massive ice avalanches on Iapetus mobilized by friction reduction during flash heating. *Nat. Geosci.* **2012**, *5*, 574–578. [CrossRef]
112. Siebe, C.; Komorowski, J.; Sheridan, M. Morphology and emplacement of an unusual debris-avalanche deposit at Jocotitlán volcano, Central Mexico. *Bull. Volcanol.* **1992**, *54*, 573–589. [CrossRef]
113. Hazlett, R.; Buesch, D.; Anderson, J.; Elan, R.; Scandone, R. Geology, failure conditions, and implications of seismogenic avalanches of the 1944 eruption at Vesuvius, Italy. *J. Volcanol. Geotherm. Res.* **1991**, *47*, 249–264. [CrossRef]
114. Lucas, A.; Mangeney, A.; Mège, D.; Bouchut, F. Influence of the scar geometry on landslide dynamics and deposits: Application to Martian landslides. *J. Geophys. Res. Planets* **2011**, *116*, E10001. [CrossRef]
115. Zhong, L. History and enlightenment of land subsidence controlling in Tianjin City. *Chin. J. Geol. Hazard Control* **2008**, *3*, 59.

116. Zhang, M.; Yin, Y. Dynamics, mobility-controlling factors and transport mechanisms of rapid long-runout rock avalanches in China. *Eng. Geol.* **2013**, *167*, 37–58. [CrossRef]
117. Yin, Z.; Xu, Y.; Zhao, W. SanXi village landslide in DuJiangyan, SiChuan province on July 10, 2013. *J. Eng. Geol.* **2014**, *22*, 309–318. [CrossRef]
118. Zhang, Y.; Xu, Q.; Peng, D.; Zhao, K.; Guo, C. An experimental study of the permeability of the catastrophic landslide at the Shenzhen landfill. *Hydrogeol. Eng. Geol.* **2017**, *44*, 131–136+149. [CrossRef]
119. Chen, J.; Chen, R.; Mi, D.; Zheng, X.; Gao, C. Kinematic processes and fragmentation characteristics of walai rock avalanche landslide in Tibet. *Adv. Eng. Sci.* **2020**, *52*, 30–39. [CrossRef]
120. Yao, Y.; Gao, C.; Cui, J.; Wang, S.; Deng, J.; Yang, Z. Numerical simulation of the movement characteristics of the nixu long-runout landslide. *J. Lanzhou Univ. Nat. Sci.* **2021**, *57*, 767–774+782. [CrossRef]

**Disclaimer/Publisher's Note:** The statements, opinions and data contained in all publications are solely those of the individual author(s) and contributor(s) and not of MDPI and/or the editor(s). MDPI and/or the editor(s) disclaim responsibility for any injury to people or property resulting from any ideas, methods, instructions or products referred to in the content.